Cyclic Deformation of FCC Crystals

by

Chuang-Chia LIN

B.S. in Mechanical Engineering,
National Taiwan University, 1990

Submitted to the Department of Mechanical Engineering
in partial fulfillment of the requirements for the degree of

Master of Science in Mechanical Engineering

at the

MASSACHUSETTS INSTITUTE OF TECHNOLOGY

January 1995

Author .....
Department of Mechanical Engineering
January 5, 1995

Certified by .....
Lallit Anand
Professor of Mechanical Engineering
Thesis Supervisor

Accepted by .....
Ain Sonin
Chairman, Departmental Committee on Graduate Students

Cyclic Deformation of FCC Crystals

by

Chuang-Chia LIN

B.S. in Mechanical Engineering,

National Taiwan University, 1990

Submitted to the Department of Mechanical Engineering
on January 5, 1995, in partial fulfillment of the
requirements for the degree of

Master of Science in Mechanical Engineering

Abstract

A combined experimental-computational program is conducted to develop a new crystal plasticity based constitutive model to predict the elastic-plastic deformation of fcc polycrystals under multi-axial cyclic loading. Uni-axial strain and stress controlled cyclic tests along with multi-axial displacement controlled cyclic tests are performed on OFHC copper. As compared to the previous phenomenological cyclic plasticity models, this physically based combined isotropic-kinematic hardening crystal plasticity model demonstrates better agreement with experiments.

Thesis Supervisor: Lallit Anand
Title: Professor of Mechanical Engineering

Acknowledgments

The first person I would like to thank is my advisor Professor Lallit Anand, a great thinker and a pioneer in the field of computational mechanics, for his guidance and support during the last two years. I also thank Professor Ali S. Argon for his excellent course which inspires my deep interest in materials behavior.

I also express my sincere appreciation to my girl friend, Liping Li, for all the support she gave me. Another special thanks goes to Dr. Christine Allan for the numerous discussions and helps she kindly initiated. Thanks to Don Fitzgerald for giving me so many friendly advises about machining and testing which I will always keep in mind. I also thank Dr. Jian Cao, Manish Kothari, Srihari Babrasupramanian, Dr. Hyungyil Lee, Dr. Fred Haubensak, Clearance Chui, Brian Gally, Surya Ganti, Alex Staroselsky, Hong Dai, Ming Zhou, John Zaroulis, Deborah Demania, and Lisa Tegeler for all their help.

Without many wonderful dinners with my best friends and former classmates, Kuo-Chang Chen and Kuo-Chun Wu, life in MIT would be further difficult. I am also grateful for Tian-Shiang Yang, Tong-Chien Tseng, Tomas Chao, Cynthia Chuang, Chen-An Chen and all other friends in ROCSA.

From dream to reality, I became a student of MIT. In the past seven hundred days, I have taken courses, made new friends, and tried to gradually melt myself into this new cultural environment. But the main subject which occupies my mind day by day, is the research work which leads to the superalloy model and this thesis. I would like to dedicate this thesis to the most important people in my life, my parents Chi-Fa Lin and Kung-Wei-Bao Lin, with my deepest gratitude and truest love.

Contents

List of Figures

List of Tables

Chapter 1

Introduction

1.1 Motivation

The development of mathematical models which describe and predict the deformation of metals is proceeding with increasing vigor. One of the existing features of the recent thrust toward plasticity modeling is its effort to bring together the separate disciplines of materials science and solid mechanics. This unification is motivated by recognition of the complexity and scope of the modeling activity. In order to provide an extrapolative and predictivitive capability, a strong physical basis is introduced into the modeling; and the multiaxial stress-strain relationship is expressed in an appropriate tensorial form. Multiaxial experimental work is conducted to determine the material parameters. Finally, numerical methods are developed to solve complex boundary values problems encountered in engineering design. Such interdisciplinary research allows development of constitutive models which comprehend and are founded on a strong physical basis, and also satisfy the requirement of a practical continuum theory.

A good example of the results of such an interdisciplinary approach is the polycrystal model developed by Anand, Kaladindi, and Bronkhorst (1991). They were the first to report a simulation and the corresponding comparison against experiments of the evolution of crystallographic texture in a non-homogeneous deformation processing operation, by using a Taylor-type polycrystal model at each integration point of a finite element mesh. A satisfactory agreement with experimental load-displacement curve and texture evolution was obtained. The advantage of using a crystal plasticity approach in modeling metal deformation is indicated by such success.

Indeed, a proper constitutive model is at the core of plasticity theory. However, a crystal plasticity model with only one internal resistance variable (Kalindindi, *et al.*,1991) has its limitations when applied to cyclic loading conditions. Their model is summarized below.

To simulate polycrystal deformations, we need to include enough grains with different orientations at each "material point". For a polycrystal materials, we assume that all grains have equal volume, and the local deformation gradient in each grain is homogeneous and identical to the macroscopic deformation gradient $\mathbf{F}$ at the continuum material point level. These assumptions leads to

$$\bar{\mathbf{T}} = \frac{1}{N} \sum_{k=1}^{N} \mathbf{T}^{(k)} \tag{1.1}$$

where $\bar{\mathbf{T}}$ is the averaged stress, N is the total number of crystals at the material point, and $\mathbf{T}^{(k)}$ is the Cauchy stress in the kth crystal.

For each grain the constitutive equation for stress is taken as

$$\mathbf{T}^* = \mathcal{L}\left[\mathbf{E}^*\right] \tag{1.2}$$

with

$$\mathbf{E}^* = \frac{1}{2}\left\{\mathbf{F}^{*^T}\mathbf{F}^* - 1\right\}, \tag{1.3}$$

$$\mathbf{T}^* = \mathbf{F}^{*^{-1}}\left\{(\det \mathbf{F}^*)\,\mathbf{T}\right\}\mathbf{F}^{*^T}, \tag{1.4}$$

and $\mathcal{L}$ a fourth order elasticity tensor. The strain and stress measure $\mathbf{E}^*$ and $\mathbf{T}^*$ are elastic work-conjugate strain and stress measures, with $\mathbf{T}$ the Cauchy stress tensor in each grain, and $\mathbf{F}^*$ the local elastic deformation gradient defined by

$$\mathbf{F}^* = \mathbf{F}\mathbf{F}^{p^{-1}}, \tag{1.5}$$

where $\mathbf{F}$ and $\mathbf{F}^p$ are the local deformation gradient and local plastic deformation gradient, respectively. In order to satisfy the condition of plastic incompressibility, $\det \mathbf{F}^p$ should equal unity.

The plastic deformation gradient is in turn given by the flow rule

$$\dot{\mathbf{F}}^p = \mathbf{L}^p\mathbf{F}^p \tag{1.6}$$

$$\mathbf{L}^p = \sum_\alpha \dot{\gamma}^\alpha \mathbf{S}_0^\alpha, \qquad \mathbf{S}_0^\alpha \equiv \mathbf{m}_0^\alpha \otimes \mathbf{n}_0^\alpha \tag{1.7}$$

where $\mathbf{m}_0^\alpha$ and $\mathbf{n}_0^\alpha$ are time-independent orthonormal unit vectors which define the slip direction and the slip plane normal of the slip system α in a fixed reference configuration. The plastic shear rate on the slip system α is denoted by $\dot{\gamma}^\alpha$, and is defined in terms of the resolved shear stress τ^α, and deformation resistance s^α:

$$\dot{\gamma^\alpha} = \hat{\dot{\gamma}}^\alpha \left(\tau^\alpha, s^\alpha\right). \tag{1.8}$$

The resolved shear stress τ^α is obtained from balancing plastic stress power per unit volume in the isoclinic relaxed configuration (e.g. Anand 1985)

$$\dot{w}^p \equiv (\mathbf{C}^*\mathbf{T}^*) \cdot \mathbf{L}^p, \qquad \text{with} \qquad \mathbf{C}^* \equiv \mathbf{F}^{*^T}\mathbf{F}^* \tag{1.9}$$

Using the above equations, we defined a resolved shear stress τ^α for the slip system α through the relation

$$\dot{w}^p = \sum_\alpha \tau^\alpha \dot{\gamma}^\alpha \tag{1.10}$$

which yields

$$\tau^\alpha \equiv (\mathbf{C}^*\mathbf{T}^*) \cdot \mathbf{S}_0^\alpha \tag{1.11}$$

Since $\mathbf{C}^*$ is approximately unity for small elastic stretches (which is true for metallic materials), we have

$$\tau^\alpha \approx \mathbf{T}^* \cdot \mathbf{S}_0^\alpha. \tag{1.12}$$

With s^α representing the deformation resistance, the hardening rule is taken as

$$\dot{s}^\alpha = \sum_\beta h^{\alpha\beta} \left|\dot{\gamma}^\beta\right|, \qquad h^{\alpha\beta} = q^{\alpha(\beta)} h^{(\beta)} \qquad \text{no sum on } \beta \tag{1.13}$$

where $q^{\alpha\beta}$ represents the latent hardening matrix. Following Asaro and Needlemen (1985),

for the 12 slip systems of FCC crystals, we have

$$\left[q^{\alpha\beta}\right] = \begin{bmatrix} \mathbf{A} & q\mathbf{A} & q\mathbf{A} & q\mathbf{A} \\ q\mathbf{A} & \mathbf{A} & q\mathbf{A} & q\mathbf{A} \\ q\mathbf{A} & q\mathbf{A} & \mathbf{A} & q\mathbf{A} \\ q\mathbf{A} & q\mathbf{A} & q\mathbf{A} & \mathbf{A} \end{bmatrix}, \tag{1.14}$$

here q is the ratio of latent hardening effect to the self hardening effect and $\mathbf{A}$ is a matrix fully populated by ones.

For the h^β, motivated by Brown, Kim and Anand (1989), we take the following form

$$h^\beta = h_0 \left(1 - \frac{s^\beta}{s_s}\right)^a. \tag{1.15}$$

From the above equations, we see that the hardening rule for s^α in a single slip deformation process with no latent hardening will be

$$\dot{s^\alpha} = h_0 \left(1 - \frac{s^\alpha}{s_s}\right)^a \left|\dot{\gamma^\alpha}\right|. \tag{1.16}$$

This equation for $\dot{s^\alpha}$ will lead to two response characteristics which are at variance with what is known about cyclic deformation:

1. Because s^α is monotonically increasing, there would be no *Bauschinger effect* – no reduction of reverse yielding strength – during reversal.

2. Irrespective of the cyclic strain amplitude, the saturation level, s_s, will be the same for all tests.

Fig. 1-1 and Fig. 1-2 show the prediction of two strain controlled tests (ϵ_a=0.75% and 1.5%) of polycrystal copper using the model of Kalindindi, *et al* with latent hardening. Although the initial monotonic stress-strain response is captured by the model very well, the prediction for the subsequent cyclic response does not match the experimental results. Therefore, the applicability of the previous model has to be restricted to monotonic deformations or to a small number of reversals. To overcome this weakness, it is required to modify the hardening rule and incorporate additional internal variables to better represent the slip system deformation resistance.

As is well known, one major factor of current incremental plasticity modelling is the

choice of appropriate internal variables and formulation of corresponding evolution equations. The issue of how many variables a good model must contain can be viewed as a question of principle versus practicality. Incorporation of all possible micro-structural variables into a model seems impractical and hard to verify. Seeking direct quantitative representation of micro-structure is also difficult. However, to provide an extrapolative capability it is required to incorporate internal variables derived from, or at least those that reflect, the internal structure. Also, these variables must be operationally defined to be measurable from physical experiments. Since a one internal variable model fails to represent cyclic deformation phenomena, in what follows we try two internal variables to characterize cyclic deformation. A common choice is the pair (s^α, x^α) where s^α is a deformation resistance and x^α is a "back stress" variable. This choice has proved useful in several previous attempts at cyclic crystal plasticity modelling applications (Stouffer 1992; Walker 1991; Teodosiu 1992). A flow rule generally accepted in these plasticity models is:

$$\dot{\gamma}^\alpha = \begin{cases} 0 & \text{if } |\tau^\alpha - x^\alpha| \leq s_{th}, \\ \dot{\gamma}_0 \left(\frac{|\tau^\alpha - x^\alpha| - s_{th}}{s^\alpha} \right)^{\frac{1}{m}} \operatorname{sign}(\tau^\alpha - x^\alpha) & \text{, otherwise.} \end{cases} \tag{1.17}$$

Here x^α is the back stress for slip system α, and s_{th} corresponds to a certain threshold resistance for all slip systems (for details see next chapter). The main difference between various models lies in the evolution equations for s^α and x^α.

To make intelligent judgment and to extract physical laws from experimental observations are the core characteristics of a successful model. In the light of this point, we begin with a brief review of previous research about the underlying mechanisms, and physical and macroscopic modeling for cyclic deformation. For a good review up to 1988, see White (1988).

1.2 Previous works

After Johann Bauschinger (1876-1886) reported the reduction of yield stress upon reversal of straining - the *Bauschinger effect*, the cause for such "anomalous" behavior had remained mysterious for almost a century. The early suggestion around 1950's was that the Bauschinger effect is developed from plastic incompatibility between deforming grains. Acknowledging the fact that the Bauschinger effect is independent of grain size (Wolley,

1953), and exists even in single crystals (Marukawa and Sanpei 1971), we can conclude that the plastic incompatibility is not the only mechanism. Since for a single crystal of pure metal the main resource for shearing resistance is dislocation interaction with cells and tangles, the cause for the reduction of reverse yield should be due to the alteration of these micro-structural features.

Hasegawa, Yakou, and Karashima (1975) conducted experiments on polycrystal aluminum and observed that dislocation cells, formed during prestraining, were dissolved at the initial stage of the reversed straining (Fig. 1-3). The overall dislocation density decreased by about 16% before increasing again. A similar result is also reported by Christodoulou, Woo, and MacEwen (1986) for polycrystal copper (Fig. 1-4). These structural changes are considered to be the origin of the Bauschinger effect in single phase metallic single crystals in which cells or subgrains are formed during pre-straining.

This partial disintegration of cell walls and dislocation tangles was later studied by Hasegawa and Kocks (1979) and Hasegawa and Yakou (1980) to compare with the effects of annealing (thermo-recovery). It was found that although both thermo-recovery and stress reversal reduce reverse yielding, their physical background and subsequent macroscopic response are different. The thermo-recovery will tighten the cell walls, *clean up* the interior of cell, and eventually lead to annihilation of dislocations inside the cell walls. On the contrary, the reverse shearing will diffuse the cell wall (Fig. 1-5), make the micro structure similar to that of a less deformed material. Macroscopically, thermo-recovery reduces the reverse yielding stress more and in a uniform way but reversal shearing shows a transient, low hardening rate region (Fig. 1-6).

The comparison between the mechanisms for annealing and strain reversal reveals one piece of information: the dislocation structure could be divided into two categories: the one which is polarized and relatively unstable and the one which is isotropic and relatively stable. While annealing will eliminate both of them, the strain reversal would only annihilate the polarized one temporarily. This concept is quite useful for constructing cyclic constitutive models.

A reversal of strain in uniaxial cycling should be considered only a special case of a general loading process. With a lot of work focusing only on the Bauschinger effect in uniaxial cyclic loading, few people have noticed that the mechanism for the Bauschinger effect should also have an influence on any complex loading path change. Such a correlation

between the Bauschinger effect, load path change test, and micro-structure was recently investigated by Rauch and Schmitt (1989). They performed two-step tests on thin plate samples of mild steel. In the first step, they deformed the samples in tension; then, they performed simple shear tests on those predeformed sample with different angle (α) between the shear and the tensile directions (Fig. 1-7). They showed that when α equals 90^o the yield stress is maximized and higher then forward flow stress, and when α equals 135^o, a test similar to the typical Bauschinger test, the opposite is true (Fig. 1-8). The augmentation of yield stress when α equals 90^o is explained by the observed formation of micro bands due to newly activated slip systems, and yield stress decrease ($\alpha = 135^o$) is, again, related to the dissolution of dislocation cell walls due to reversed shear stress on the same slip systems. What has been indicated by Rauch and Schmitt is the importance of the role of slip activity and the dissolution of dislocation cell structure upon reversal of slip on the same slip system.

The above experimental observations indicate that the deformation resistance, which could be expressed in terms of dislocation density, will not simply increase monotonously. In reality, the dislocation density will decrease during reversal, and this phenomenon is the cause for Bauschinger effect and related material behavior in a cyclic deformation process of pure single phase metallic crystal. Based on such an idea, White, Bronkhorst and Anand (1990) reported a phenomenological plasticity model with two internal variables, namely, deformation resistance and back stress. They also compared simulations of the model to uniaxial cyclic test data on five different materials – 1100-O Aluminum, 316 stainless steel, and spherodized 1020, 1045 and 1095 plain carbon steels. The model was shown to capture the key features of these uniaxial cyclic behavior reasonably well.

A similar, but more complicated model was later on reported by Hu, Rauch and Teodosiu (1992). Based on the idea that the dislocation cell walls are polarized (Kocks, 1980), they separate the deformation resistance into three parts, (P, R, X). The part P is polarity dependent and is related to persistent dislocation structures, the part R is related to rearrangement and formations, and the part X is related to less stable dislocation arrangements. This model may be viewed as an extension of the model by White and Anand, but in a more complicated form. Their continuum plasticity model simulations match their large strain torsion tests data on AK-mild steel quite well.

In the framework of crystal plasticity for cyclic loading, the main focus has been on ap-

plication to single crystal superalloys. Stouffer and co-workers (1988, 1990, 1992) have proposed crystal plasticity models based on the idea of back stress. Walker and Jordan (1989, 1992) and Meric and Cailetlaud (1991) also present their combined isotropic-kinematic hardening model for superalloy PWA1480, and SNECMA AM1, respectively. Although there are complexities such as non-Schmid effect and temperature dependence in modeling superalloys, the small isotropic hardening of these highly strengthened two-phase materials usually allows simple isotropic hardening rules, such as non-hardening. Therefore, these models are not directly applicable to non-strengthened materials showing both hardening and softening in cyclic deformation.

Weng (1979, 1980, 1987) was one of the first to study kinematic hardening in cyclic loading in terms of crystal plasticity, and he approached this problem in a different way as compared to the other researchers. He consider the forward and reverse slip system as two different ones, and treated the Bauschinger effect as a latent hardening effect. Instead of using a single latent hardening ratio q (Equation 1.14), he express the latent hardening matrix $q^{\alpha\beta}$ as:

$$q^{\alpha\beta} = q_1 + (1 - q_1)\cos\theta^{\alpha\beta}\cos\phi^{\alpha\beta} + \left(q_2 \sin\theta^{\alpha\beta} + q_3 \sin\phi^{\alpha\beta}\right) \tag{1.18}$$

where $\theta^{\alpha\beta}$ is the angle between the slip direction and the αth and βth systems, and $\phi^{\alpha\beta}$ the angle between their slip plane normals. The three parameters q_1, q_2, and q_3 are to be determined by latent hardening tests. With this interaction hardening matrix, he was able to reasonably match the latent hardening tests by Edward and Washburns (1954). His predictions of yield surface test of Philips and Tang (1972) were also good. Compared to the back stress models using simple latent hardening matrix (Eqn. 1.14), this approach may have some merit. However, such geometric based relationship can still not fully characterize the nature of the hardening interactions. Besides, its application is more limited due its complicated slip interaction relations, and more tests are required to define the extra parameters such as q_1, q_2, and q_3.

It is worth noting that there is another branch of cyclic plasticity models – the so-called two surface models – which have been developed by some workers in the last thirty years (e.g. Sierakowski, 1965; Morz, 1967, 1983; Dafalias and Popov, 1975, 1976). The general idea is to create one more (or multiple) bounding surfaces in addition to the yield surface in

stress space. The performance of such models depends on their specific equations specifying the translation and expansion of these bounding surfaces, and generally improves with the increasing number of surfaces or complexity of the specific equations. The latest model of this type is from Hassan and Kyriakidas (1994), which shows a good match with most of their uniaxial and biaxial ratcheting experiments on 304 and 1018 steels. However, they have to use different set of equations to reproduce the biaxial test than those they use for uniaxial tests. Also, their model is fairly complicated.

The general shortcomings of these two-surface phenomenological models lies in their lack of adaptability for extension to model anisotropic or inhomogenous materials, for instance, pre-textured polycrystals, two phase materials, or single crystals. It is also hard to reconcile these model for high temperature applications due to their rate-independent nature.

Recently, Khan and Su (1994) combined the latent hardening from Weng (1987), the forest dislocation relation from Jackson and Basinski (1967) and two-surface model similar to Dafalias and Popov (1976), and created a set of new constitutive relations for single crystals. They did a good job in matching the latent hardening test data of Edward *et al.* (1954) and Tang *et al.* (1972), but no prediction for multiple slip deformation is reported. Unlike the old two-surface models, some physical connections to dislocation densities and resolved shear stress are made to obtain equations for the bounding surfaces. This approach brings new insight to view the hardening mechanisms from constitutive modeling, but their lengthy formalism for more complicated slip activity seems to lack practicality.

1.3 Objective

With continuing efforts from researchers around the world, the picture of a general plasticity model has become more clear than ever before. Although there are no general guidelines for constructing such constitutive models, a crystal plasticity model with combined isotropic hardening and kinematic hardening, or in terms of internal variables, a deformation resistance and a backstress, seems to be a balanced choice between complexity and practicality for modeling of general deformations of metallic materials. Moreover, good multiaxial experimental data have been lacking and most current phenomenological models show moderate predictability for multiaxial test results. Accordingly, an experimental-computational program is conducted to develop such a combined isotropic-kinematic hardening crystal

plasticity model. Appropriate specific constitutive equations are constructed based on critical uniaxial/biaxial experiments with the objective of capturing the following important material behavior (White, Bronkhorst and Anand 1990):

1. Monotonic deformations:

- At low superposed pressures, initial yield and strain hardening are generally the same for uniaxial tensile or compressive deformation.

- If geometrical instabilities are suppressed, then strain hardening may continue to many hundred percent strain.

2. Uniaxial reversed and cyclic deformation:

- The *Bauschinger effect*: after deformation in one direction a reversal in the direction of deformation shows a reduced stress magnitude when yielding occurs again. There is usually a smooth transition from elastic to elastic-plastic behavior upon development of plastic flow in the reverse direction. As the tangent modulus gradually decreases and achieves the value it had prior to unloading, there may be a "permanent softening" where the flow stress magnitude is less than it would have been in unidirectional loading at the same accumulated strain. (Fig. 1-9)

- Under symmetric cycles of strain (or stress) metals in a annealed state will harden cyclically and tend to stable limit cycle (Fig. 1-1 and 1-2), while those in a cold worked condition will soften to a stable cycle.

- *Unsymmetric cycles of stress* in the plastic range will cause progressive "creep" or "ratcheting" in the direction of the mean stress. Depending on the material, the strain increment might stabilize during ratcheting, or becomes unstable as in Fig. 1-10.

- *Unsymmetric cycles of strain* for cold worked metals in the plastic range will cause progressive relaxation to zero of the mean stress in the cycle. For annealed metals, the material will harden cyclically to a stable loop as in the symmetric strain cycling case. Softening might appear as the annealed material is continued to be cycled to large number of cycles, or in a multi-step unsymmetric strain cycling test (Fig. 1-11).

3. Small strain multiaxial cyclic deformation:

- *Proportional* cycles of combined tension-torsion for a given equivalent strain amplitude gives rise to an "equivalent" cyclic stress-strain response which is the same as that obtained in uniaxial strain cycling for the same strain amplitude.

- *Non-proportional* tension-torsion cycling exhibits higher hardening and higher saturation stress levels for cycling to the same maximum equivalent strain amplitude as compared to proportional cycling (Fig. 1-12). The combined out-of-phase tension-torsion test with a phase difference of 90 degrees causes the largest cyclic hardening of all possible paths with the same strain range.

In the following chapters, we present the results of the current study with the objective of capturing the above criteria. Attension is first focused on the constitutive equations, which, combined with time-integration schemes, will be introduced in the next chapter.

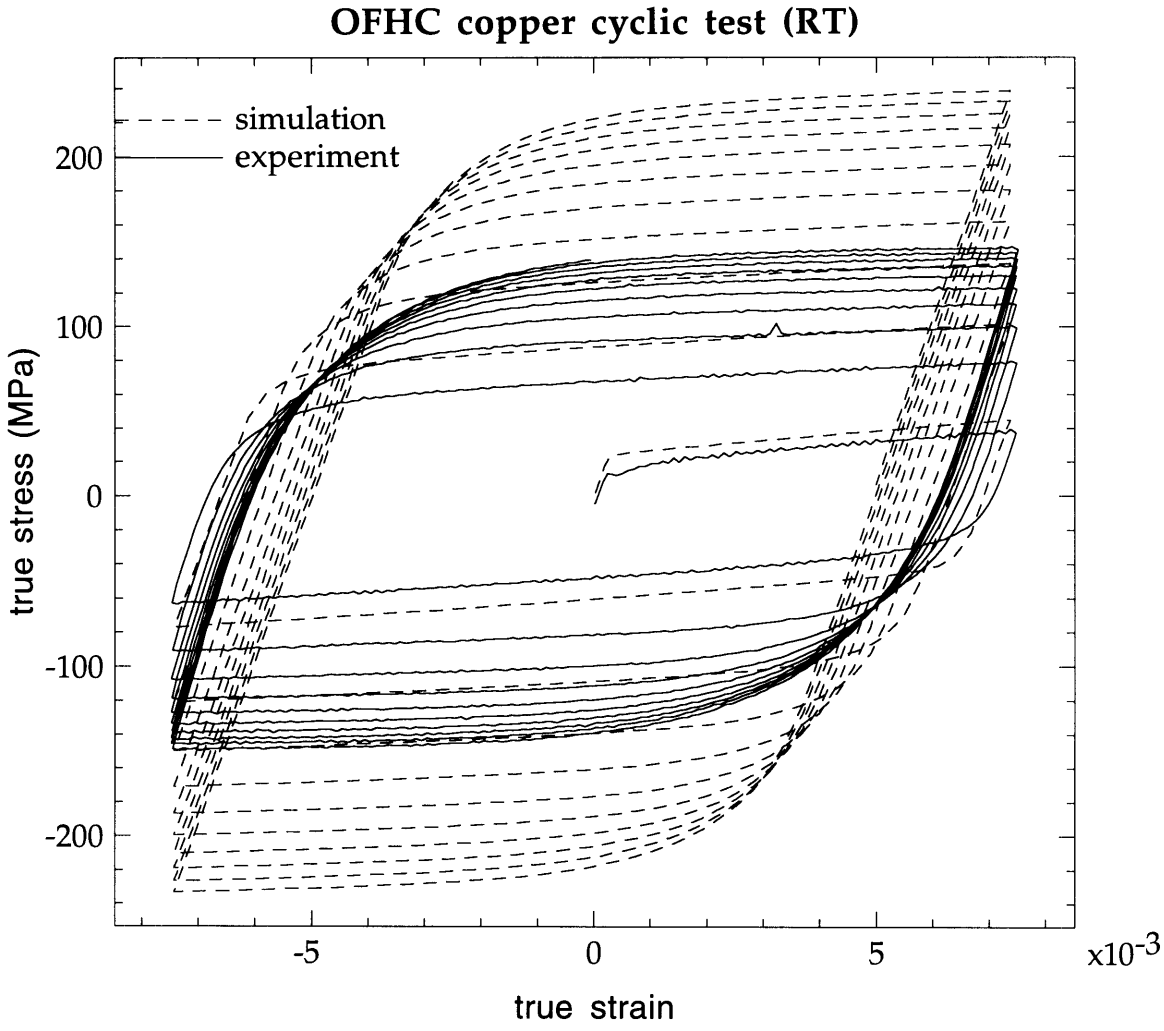

Figure 1-1: Prediction of symmetric strain cyclic test with model of Kalindindi, Bronkhorst, and Anand, $\epsilon_a = 0.75\%$.

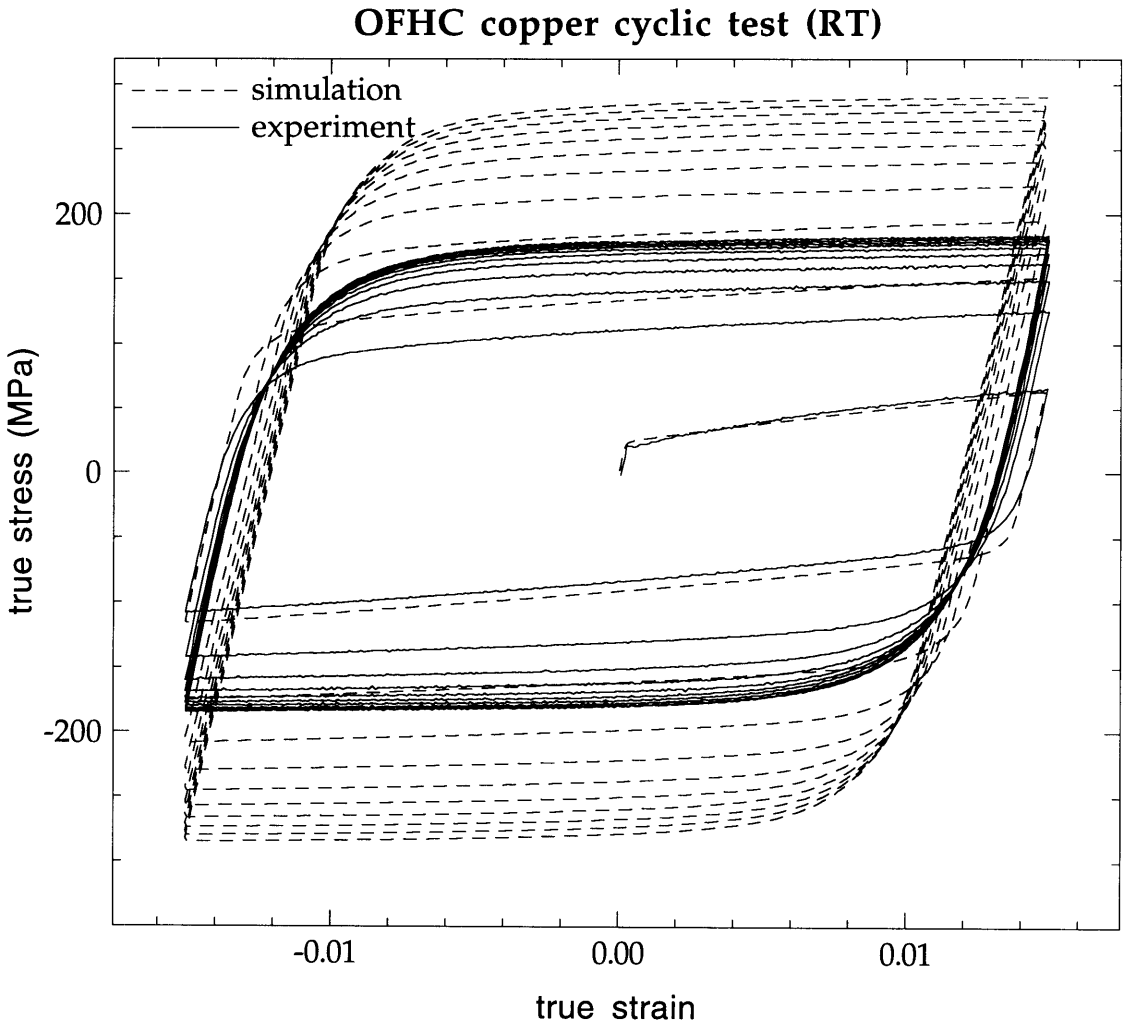

Figure 1-2: Prediction of symmetric strain cyclic test with model of Kalindindi, Bronkhorst, and Anand, $\epsilon_a = 1.5\%$.

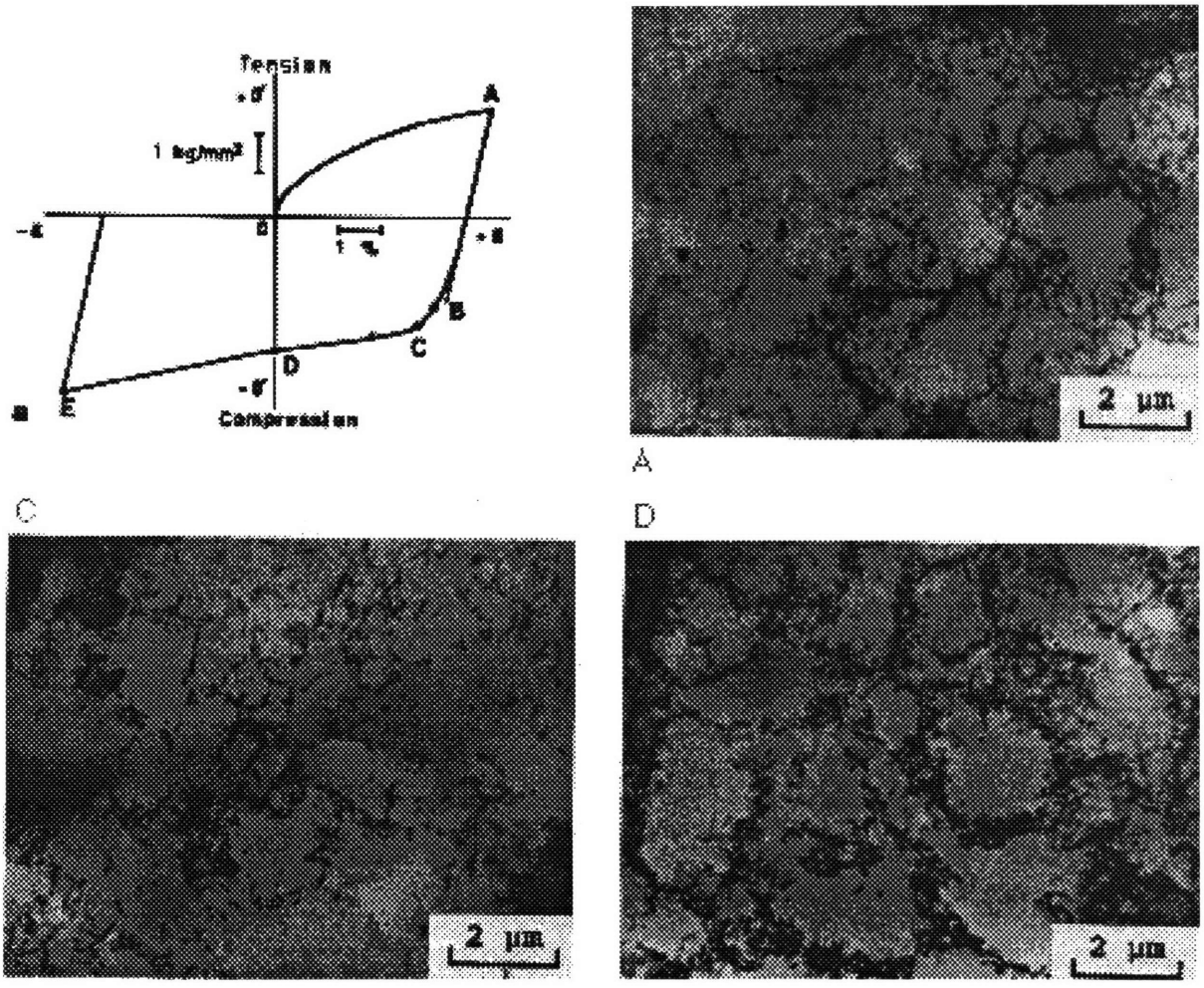

Figure 1-3: TEM pictures from Hasegawa and Yakou (1975). Dislocation density decreases at the initial stage of reversal (point C)

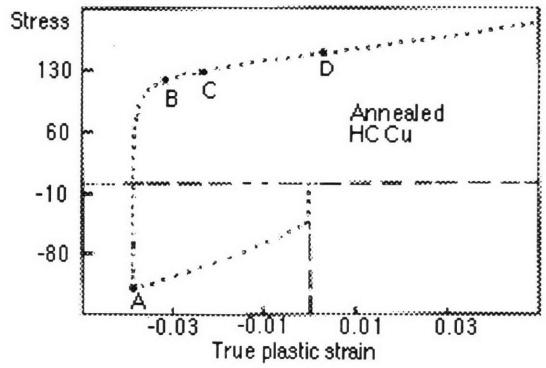

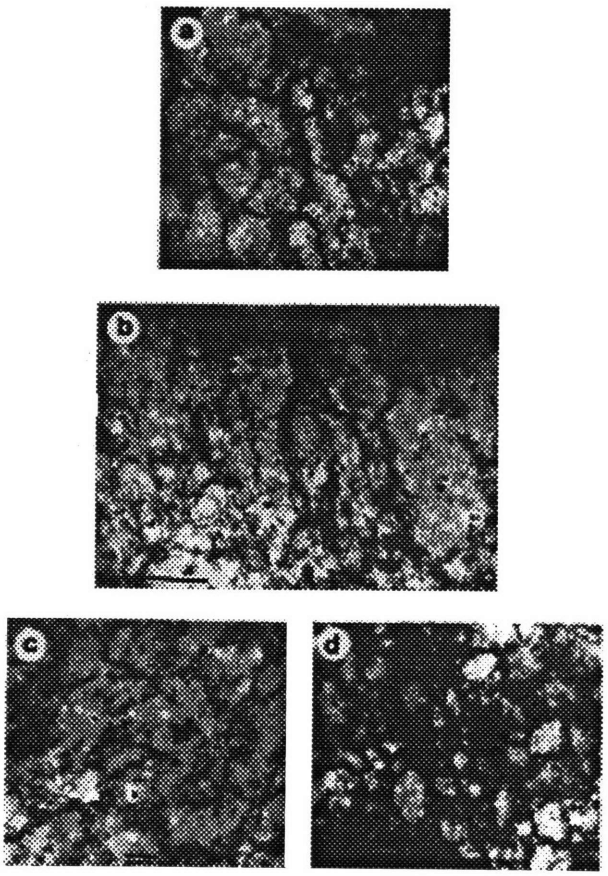

Figure 1-4: Dislocation dissolution during reversal (Christodoulou et al. 1986)

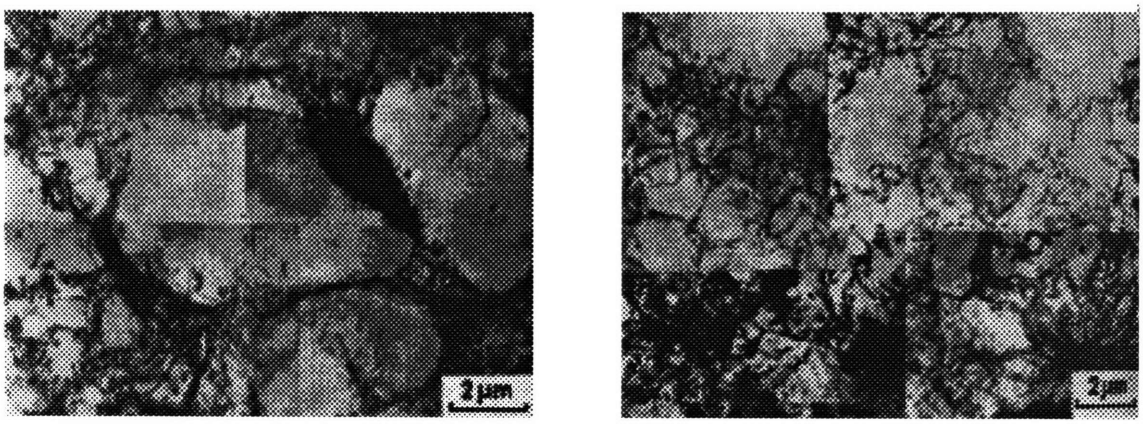

Figure 1-5: HVEM pictures shows diffusion of dislocation cell walls and tangles during strain reversal. The left picture is taken before reversal, the right one is after. (Hasegawa and Yakou, 1980)

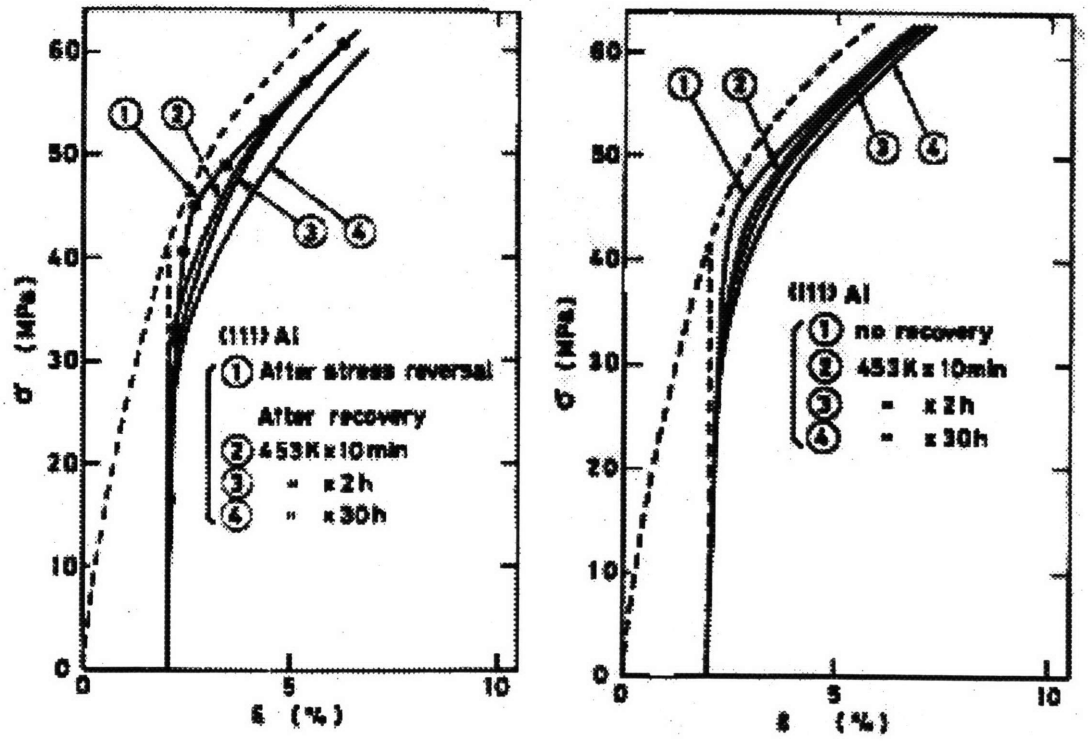

Figure 1-6: Stress strain response of reverse loading before and after annealing. The one on the left compares reverse loading to forward loading after annealing, the curves on the right are all from reverse loading (Hasegawa and Yakou, 1980)

STAGE 1. TENSION ON LARGE PLATE SAMPLE

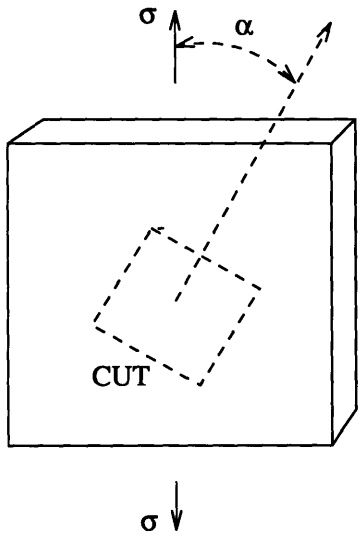

STAGE 2. SHEAR ON SMALL CUT SQUARE SAMPLE

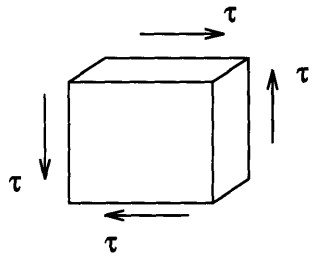

Figure 1-7: Two-stage strain path change test (Rauch and Schmitt, 1989)

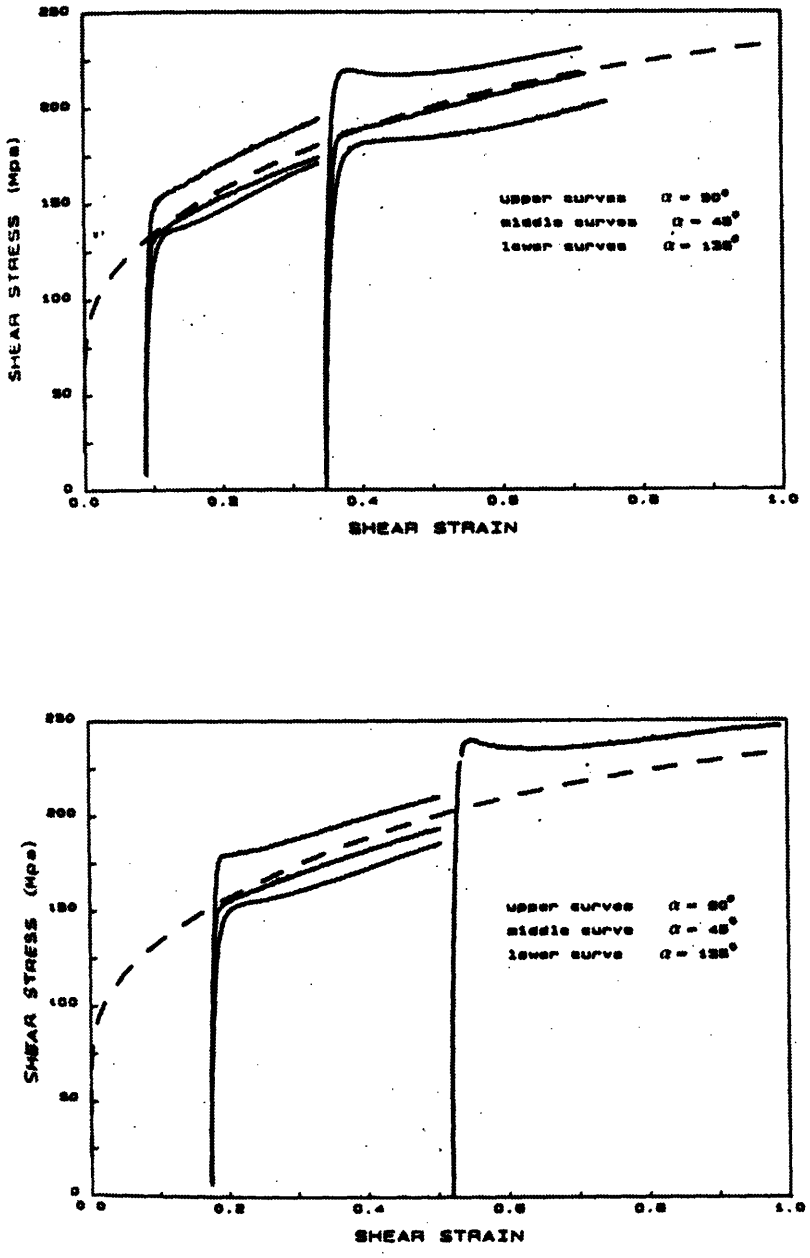

Figure 1-8: Stress strain response for loading path change test. (Rauch and Schmitt, 1989)

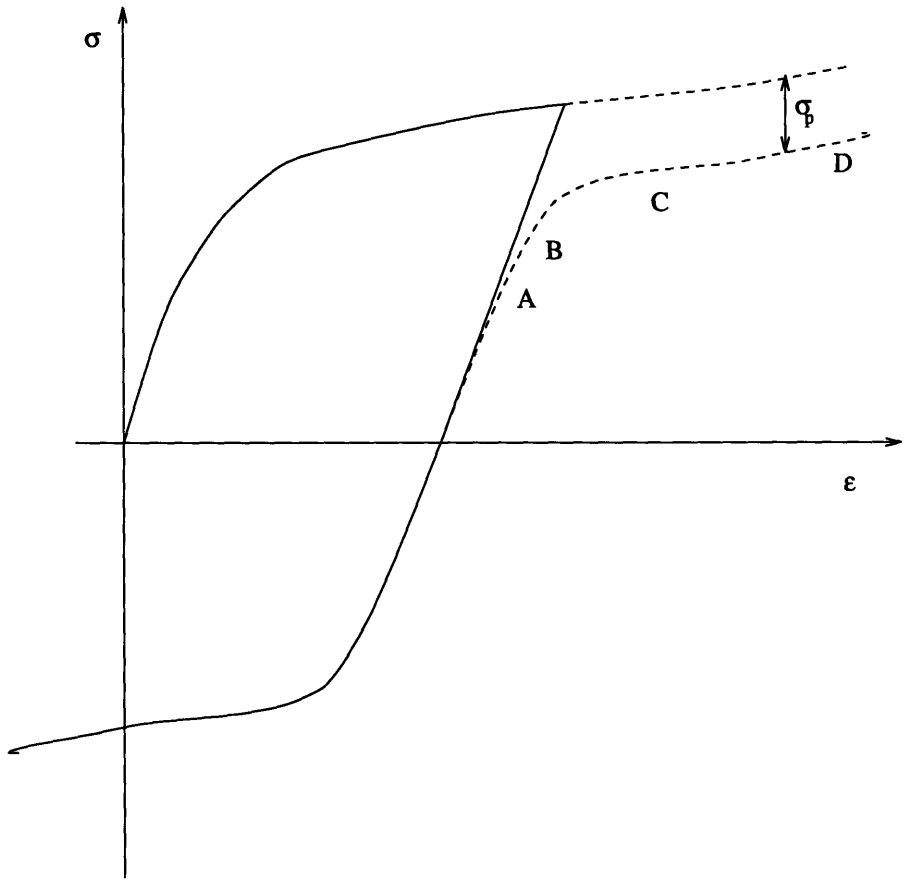

Figure 1-9: Schematic drawing shows the typical Bauschinger effect. Compared to the forward curve, there are: A. reduction of reverse yielding strength; B. smooth transition showing a strong hardening region; C. low hardening region; D. An offset in stress level (permanant softening σ_p).

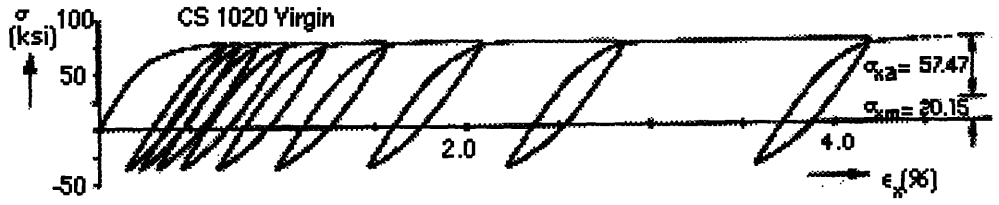

Figure 1-10: Unstable ratcheting of CS 1020 steel due to cyclic softening (Hassan and Kyriakidas, 1994)

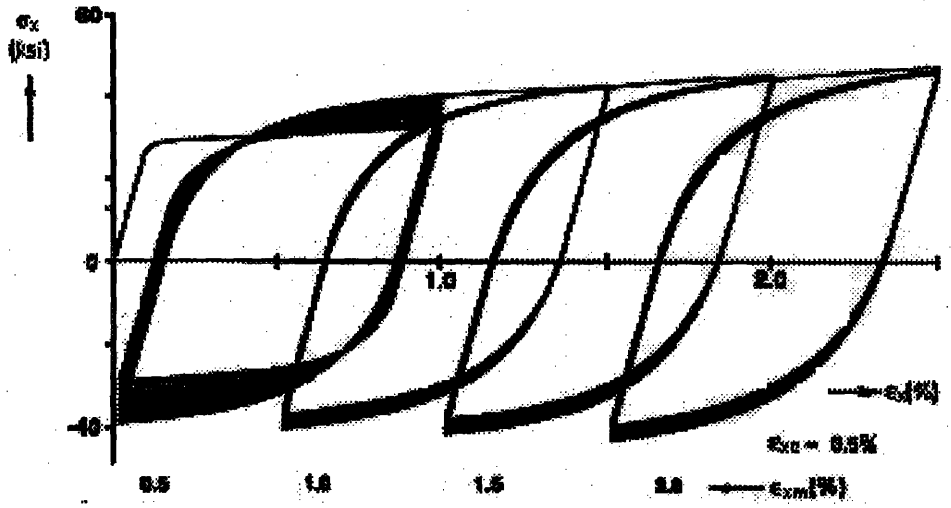

Figure 1-11: Four step unsymmetric strain cycling performed on SS 304 steel, the material cyclic hardened in the first step, and showed slight relaxation in the last two steps (Hassan and Kyriakidas, 1994)

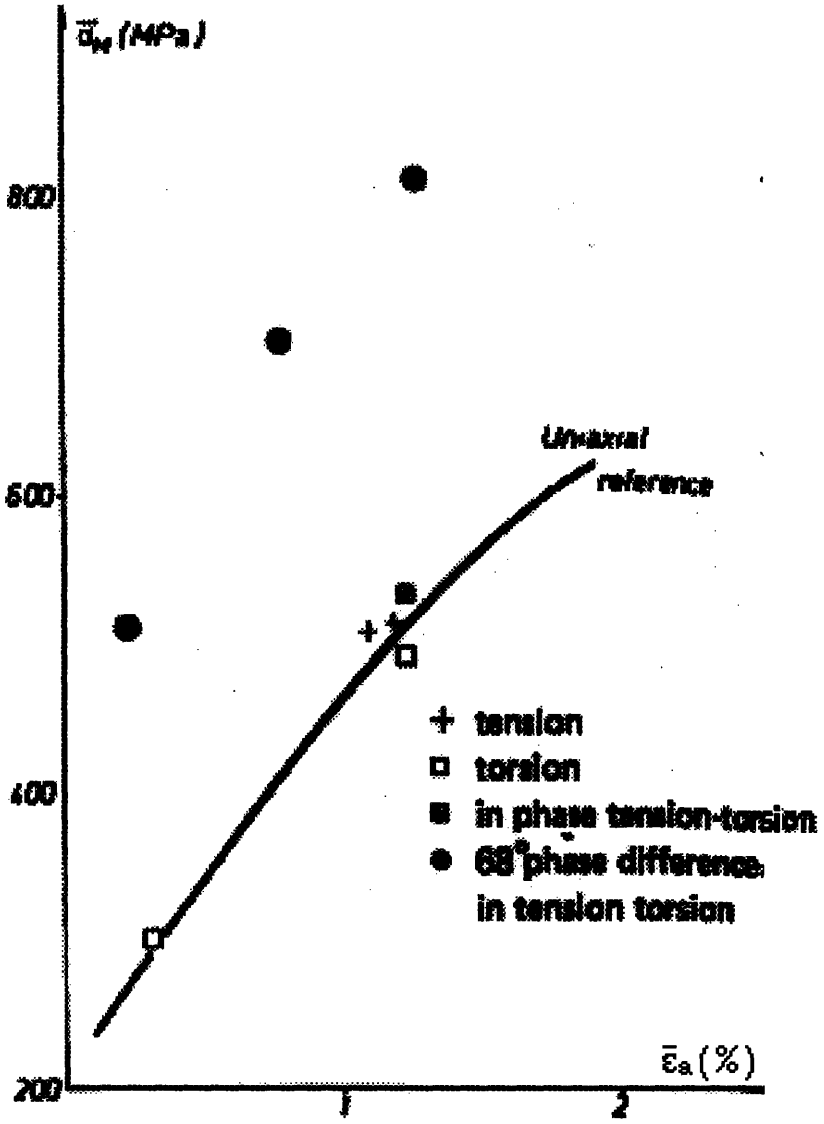

Figure 1-12: Tension, torsion, and combined-tension/torsion tests with different phase lags on 316 SS plotted on the saturation equivalent stress-equivalent strain amplitude axis. It shows that the non-proportional cycling leads to higher saturation stress. (Cailletaud *et al.*, 1984)

Chapter 2

Combined Isotropic-Kinematic Hardening Polycrystal Model

The present work extends the polycrystal visco-plasticity model of Anand and co-worker (Bronkhorst *et al.*, 1991 and Kalindindi *et al.*,1991). Basically, in addition to the slip resistance s^α of Anand, *et al.*, we introduce another internal variable, a "back stress" parameter x^α on each slip system, and corresponding evolution equations to represent the essence of anisotropic hardening during cyclic deformation process. The slip resistance s^α is related to the forest dislocation density in a physical sense, and the directional resisting strength developed during shearing is represented by the back stress x^α. New equations for $\dot{\gamma}^\alpha$ and the evolution equations for s^α and x^α are formulated. These equations are introduced in the following sections.

2.1 Specific Constitutive Equations

For the cubic crystals considered in the current research, the description of the elasticity tensor $\mathcal{L}$ requires three stiffness parameters, C_{11}, C_{12}, and C_{44}, which are defined as:

$$C_{11} = (\mathbf{e}_1^c \otimes \mathbf{e}_1^c) \cdot \mathcal{L}\,[\mathbf{e}_1^c \otimes \mathbf{e}_1^c] \tag{2.1}$$

$$C_{12} = (\mathbf{e}_1^c \otimes \mathbf{e}_1^c) \cdot \mathcal{L}\,[\mathbf{e}_2^c \otimes \mathbf{e}_2^c] \tag{2.2}$$

$$C_{44} = (\mathbf{e}_1^c \otimes \mathbf{e}_2^c) \cdot \mathcal{L}\,[2\mathrm{sym}\,(\mathbf{e}_1^c \otimes \mathbf{e}_2^c)] \tag{2.3}$$

where $\mathbf{e}_i^c$ $(i = 1, 2, 3)$ denotes an orthonormal basis associated with the crystal lattice.

There are several features of a typical uniaxial cyclic stress strain relationship that we should consider while constructing the model. Initially, the reverse proportional limit is lower than the forward flow stress. Secondly, an initial high hardening rate region accompanied by a relatively long region of low hardening are usually observed, showing a plateau on the curve. Finally, as the reverse hardening rate approaches the forward hardening rate there is an offset in the stress magnitude at equal accumulated strain level. Such an offset is often referred to as "permanent softening" in the literature.

To match these features, the specific constitutive functions for the plastic shearing rate $\dot{\gamma}^\alpha$ is taken as

$$\dot{\gamma}^\alpha = \begin{cases} 0 & \text{if } |\tau^\alpha - x^\alpha| \leq s_{th} \\ \dot{\gamma}_0 \left(\frac{|\tau^\alpha - x^\alpha| - s_{th}}{s^\alpha} \right)^{\frac{1}{m}} \operatorname{sign}(\tau^\alpha - x^\alpha) & \text{if } |\tau^\alpha - x^\alpha| > s_{th}, \end{cases} \tag{2.4}$$

where $\dot{\gamma}_0$ and m are material parameters representing a reference shearing rate and shear rate sensitivity. The parameter s_{th} represents a threshold value for the effective stress $(\tau^\alpha - x^\alpha)$ below which no shearing occurs in slip system α. For pure metals, s_{th} is in the order of 0.1 Mpa. The parameter s^α is the shearing resistance, and x^α is the back stress.

Motivated by White, Bronkhorst and Anand (1990), the slip resistance s^α is taken to evolve as

$$\dot{s}^\alpha = \sum_\beta h_1^{\alpha\beta} \left| \dot{\gamma}^\beta \right| - h_2^\alpha \left| \dot{\gamma}^\alpha \right| \tag{2.5}$$

where

$$h_1^{\alpha\beta} = q^{\alpha(\beta)} h_1^{(\beta)} \qquad \text{(no sum on } \beta\text{)}, \tag{2.6}$$

and

$$h_1^\beta = \eta \left(1 - \frac{s^\beta}{s_s} \right)^a . \tag{2.7}$$

The first part of (2.5) is essentially the same as the hardening rule from the crystal plasticity model by Anand and co-workers. Here η, s_s, and a are constants, and s_s denotes the saturation value for s.

The second part in (2.5) represents the softening effect in cyclic loading. The h_2^α stands for the rate of softening on slip system α due to a reversal of shearing on that system. Previous experimental results in the literature indicate that the softening effect is active only during the "reversal transient" which is (approximately) limited to the time that it

takes for the back stress to change sign and achieve the same magnitude it had prior to the reversal. In order to properly define the softening modulus h_2^α, we generalize such an idea and operationally define the "reversal transient" and related parameters in our model as follows:

- During a cyclic loading process, a reversal transient for a slip system commences when $\dot{\gamma}^\alpha$ or the effective stress $(\tau^\alpha - x^\alpha)$ changes sign. Let t_n denote the time when the reversal transient commences, and let

$$x_*^\alpha = x^\alpha(t_n) \tag{2.8}$$

  denote the value of x^α at the beginning of the reversal event.

- A reversal transient ends when the back stress reaches the same magnitude but opposite sign as when the transient started. That is, a reversal transient ends when

$$x^\alpha(\tau) = -x_*^\alpha, \qquad \tau > t_n \tag{2.9}$$

- Let f^α denote the fraction of a reversal event the slip system has experienced. Referring to Fig. 2-1 and 2-2, f^α is defined as

$$f^\alpha \equiv \begin{cases} 0 & \text{when } (\tau^\alpha - x^\alpha) \text{ changes sign,} \\ \frac{1}{2}\left(1 - \frac{x^\alpha}{x_*^\alpha}\right) = \frac{a}{a+b} & , \\ 1 & \text{when } x^\alpha = -x_*^\alpha \quad . \end{cases} \tag{2.10}$$

We define the softening rate h_2^α based on the following ideas. We assume that h_2^α

- Vanishes as f^α approaches unity.
- Is proportional to $|x_*^\alpha|$.
- Is independent of s^α.

Accordingly, we assume that

$$h_2^\alpha = \xi\left(1 - f^\alpha\right)\left(|x_*^\alpha|\right) \tag{2.11}$$

Here ξ is taken as a constant.

In (2.11), we assume that the softening rate h_2 is proportional to the maximum opposing stress $|x_*|$. A additional inverse dependence of $(|x_*| + s_{th})$ is found necessary to correctly model the small strain cyclic response ($\epsilon_a < 0.5\%$). Numerical experiments showed that when the cyclic strain amplitude is less than 0.5%, the softening effect needs to be enhanced to more accurately reproduce the experimental data. We assume a simple inverse relationship of $|x_*^\alpha|$ to represent this observation. To prevent the singularity of this term for situations when $|x_*^\alpha| = 0$, we also included the threshold resistance s_{th} in the denominator. Based on these assumptions, the complete form for h_2^α is motivated to be

$$h_2^\alpha = \xi\,(1 - f^\alpha)\left(|x_*^\alpha| + \frac{1}{|x_*^\alpha| + s_{th}}\right) \tag{2.12}$$

This relative strong softening effect in small strain cycling may be qualitatively explained by the following arguments. In small strain cyclic deformations, planar vein structures consisting of edge dislocation bundles are observed. The existence of such planar vein structures have been verified for single crystals (e.g. Basinski, Basinski, and Howie 1969), and also individual grain of polycrystals (e.g. Liu, You, and Bassin 1994). Based on purely geometrical considerations, it seems reasonable to argue that a planar dislocation structure is easier to dissolve on reversed deformation as compared to a three dimensional cell network formed during large strain cycling. Since these planar structures mainly appear during small strain cycling, we find stronger softening during small strain cycling. To model such effect, we take a first order approach and assume h_2 to be simply inversely dependent on $|x_*| + s_{th}$. A good match between the simulation results and experimental data justifies the utility of including such a term (Chap. 3).

Next, for the evolution for the back stress we assume

$$\dot{x^\alpha} = h_3^\alpha\left(1 - \frac{x^\alpha}{x_s}\text{sign}\,(\dot{\gamma^\alpha})\right)\dot{\gamma^\alpha} \tag{2.13}$$

where h_3^α is the rate of hardening for the back stress.

As indicated in Chap.1, it has been experimentally observed that at the beginning of stress reversal, the dislocation cell walls will disintegrate (Hasegawa and Yakou, 1975) and reduce the slip resistance(s). In the mean time, the back stress also changes sign. Therefore the rate of softening for s and the rate of change of back stress are *coupled*. In this model, we choose to establish a linear relationship between h_2 and h_3, and assume the following

form for h_3

$$h_3^\alpha = \phi + \chi h_2^\alpha, \tag{2.14}$$

where ϕ and χ are constants. We will show that such correlation between h_3^α and h_2^α provides a capability to obtain a reasonable match with experimental results (Chap. 3).

The set of equations (2.4) through (2.14) is aimed at representing the major features of the flow stress evolution in a typical cyclic test. Using representative values of material parmeters, Fig. 2-3 schematically shows the evolution of τ^α, x^α, and s^α for one slip system of a single crystal undergoing single reversal. Before the reversal, the resolved shear stress reaches 40 MPa, but the reverse yield strength drops to 36 MPa. The difference between the forward the reverse flow stress is approximately equal to two times the back stress at reversal. As back stress changes sign and hardens in the other direction after reversal, there is a corresponding low hardening region for the stress and the s also softens reasonably. These three effect are coupled together through the constitutive equations introduced above.

To further examine the contribution from each terms from the constitutive equation, we invert (2.4), and we will get

$$|\tau^\alpha - x^\alpha| - s_{th} = \left(\frac{\dot{\gamma}^\alpha}{\dot{\gamma}_0}\right)^m s^\alpha \tag{2.15}$$

Let $\tau^\alpha > x^\alpha$ before reversal and assume s_{th} to be small and negligible, then

$$\tau^\alpha \approx \left(\frac{\dot{\gamma}^\alpha}{\dot{\gamma}_0}\right)^m s^\alpha + x^\alpha. \tag{2.16}$$

After reversal, the relationship becomes

$$-\tau^\alpha \approx \left(\frac{\dot{\gamma}^\alpha}{\dot{\gamma}_0}\right)^m s^\alpha - x^\alpha. \tag{2.17}$$

Taking absolute value of the above two equations, it is not hard to see that whenever τ^α changes sign, the magnitude of the reverse yield stress will be reduced by two times the value of current x^α. Accordingly, from Eqn. 2.13, we see that $\dot{x}^\alpha$ will change sign at reversal straining and its magnitude will be relatively large at the beginning before it goes down, showing a high initial hardening rate for the flow stress.

At the same time, the hardening rate s^α reduces during the reversal transient due to the increasing contribution from h_2, and we get a plateau on the stress strain curve

(Fig. 2-3). Eventually, as x^α reaches the same magnitude as before reversal (the end the reversal transient), the s^α has not hardened very much due to the softening effect during the reversal transient. Therefore, we would observe an offset between the forward and reverse stress levels - the permanent softening - on an accumulated strain-stress diagram.

Having examined the interaction between the constitutive equations for single slip, let us summarize the complete model for a single crystal as follows:

1. Constitutive Equation for Stress:

$$\mathbf{T}^* = \mathcal{L}[\mathbf{E}^*] \tag{2.18}$$

with

$$\mathbf{E}^* = \frac{1}{2}\left\{\mathbf{F}^{*T}\mathbf{F}^* - 1\right\} \tag{2.19}$$

$$\mathbf{T}^* = \mathbf{F}^{*-1}\left\{(\det \mathbf{F}^*)\,\mathbf{T}\right\}\mathbf{F}^{*-T} \tag{2.20}$$

$$\mathbf{F}^* = \mathbf{F}\mathbf{F}^{p^{-1}} \tag{2.21}$$

2. Flow rule:

$$\dot{\mathbf{F}}^p = \mathbf{L}^p\mathbf{F}^p \tag{2.22}$$

$$\mathbf{L}^p = \sum_\alpha \dot{\gamma}^\alpha \mathbf{S}_0^\alpha \qquad \mathbf{S}_0^\alpha \equiv \mathbf{m}_0^\alpha \otimes \mathbf{n}_0^\alpha \tag{2.23}$$

$$\dot{\gamma} = \begin{cases} 0 & \text{if } |\tau^\alpha - x^\alpha| \le s_{th} \\ \dot{\gamma}_0 \left(\frac{|\tau^\alpha - x^\alpha| - s_{th}}{s^\alpha}\right)^{\frac{1}{m}} \text{sign}\,(\tau^\alpha - x^\alpha) & \text{if } |\tau^\alpha - x^\alpha| > s_{th} \end{cases} \tag{2.24}$$

$$\tau^\alpha \approx \mathbf{T}^* \cdot \mathbf{S}_0^\alpha \tag{2.25}$$

3. Evolution Equations for s^α:

$$\dot{s}^\alpha = \sum_\beta h_1^{\alpha\beta}\left|\dot{\gamma}^\beta\right| - h_2^\alpha\left|\dot{\gamma}^\alpha\right| \tag{2.26}$$

$$h_1^{\alpha\beta} = q^{\alpha\beta}h_1^\beta \qquad (\textit{ no sum on } \beta\ ) \tag{2.27}$$

$$q^{\alpha\beta} = \begin{bmatrix} \mathbf{A} & q\mathbf{A} & q\mathbf{A} & q\mathbf{A} \\ q\mathbf{A} & \mathbf{A} & q\mathbf{A} & q\mathbf{A} \\ q\mathbf{A} & q\mathbf{A} & \mathbf{A} & q\mathbf{A} \\ q\mathbf{A} & q\mathbf{A} & q\mathbf{A} & \mathbf{A} \end{bmatrix}, \qquad A = \begin{bmatrix} 1 & 1 & 1 \\ 1 & 1 & 1 \\ 1 & 1 & 1 \end{bmatrix} \tag{2.28}$$

$$h_1^\beta = \eta \left(1 - \frac{s^\beta}{s_s}\right)^a \tag{2.29}$$

$$h_2^\alpha = \xi \left(1 - f^\alpha\right) \left(|x_*^\alpha| + \frac{1}{|x_*^\alpha| + s_{th}}\right) \tag{2.30}$$

$$f^\alpha \equiv \begin{cases} 0 & \text{when } (\tau^\alpha - x^\alpha) \text{ changes sign} \\ \frac{1}{2}\left(1 - \frac{x^\alpha}{x_*^\alpha}\right) = \frac{a}{a+b} & \\ 1 & \text{when } x^\alpha = -x_*^\alpha \end{cases} \tag{2.31}$$

4. Evolution Equations for x^α:

$$\dot{x^\alpha} = h_3^\alpha \left(1 - \frac{x^\alpha}{x_s} \text{sign}\left(\dot{\gamma^\alpha}\right)\right) \dot{\gamma^\alpha} \tag{2.32}$$

$$h_3^\alpha = \phi + \chi h_2 \tag{2.33}$$

2.2 Time Integration Procedure

Let t denote the current time, and $\tau = t + \Delta t$ the time at the end of an increment. Then, proceeding in a fasion similar to the time integration procedure for a polycrystal plasticity model without back stress (Kalidindi, 1992), we start from solving a set of nonlinear, simultaneous algebraic equations in $\mathbf{T}^*(\tau)$,$s^\alpha(\tau)$, and $x^\alpha(\tau)$. The equation for $\mathbf{T}^*(\tau)$ and $s^\alpha(\tau)$ is quite similar to the previous work:

$$\mathbf{T}^*(\tau) = \mathbf{T}^{*^{tr}} - \sum_\alpha \Delta\gamma^\alpha \left(\tau^\alpha \left(\mathbf{T}^*(\tau)\right), s^\alpha(\tau), x^\alpha(\tau)\right) \mathbf{C}^\alpha \quad , \tag{2.34}$$

$$s^\alpha(\tau) \;=\; s^\alpha(t) + \sum_\beta h_1^{\alpha\beta}\left(s^\beta(\tau)\right) \left|\Delta\gamma^\beta\left(\tau^\beta\left(\mathbf{T}^*(\tau)\right), s^\beta(\tau), x^\beta(\tau)\right)\right| \tag{2.35}$$

$$-h_2^\alpha\left(x^\alpha(\tau)\right)\left|\Delta\gamma^\alpha\left(\tau^\alpha\left(\mathbf{T}^*(\tau)\right), s^\alpha(\tau), x^\alpha(\tau)\right)\right|$$

where

$$\mathbf{T}^{*^{tr}} \equiv \mathcal{L}\left[\left(\frac{1}{2}\right)\{\mathbf{A}-1\}\right] \quad , \tag{2.36}$$

$$\mathbf{C}^\alpha \equiv \mathcal{L}\left[\left(\frac{1}{2}\right)\mathbf{B}^\alpha\right] \quad , \tag{2.37}$$

$$\mathbf{A} \equiv \mathbf{F}^{p^{-T}}(t)\,\mathbf{F}^T(\tau)\,\mathbf{F}(\tau)\,\mathbf{F}^{p^{-1}}(t) \quad , \tag{2.38}$$

$$\mathbf{B}^\alpha \equiv \mathbf{A}\mathbf{S}_0^\alpha + \mathbf{S}_0^\alpha\mathbf{A} \quad . \tag{2.39}$$

To obtain the equation for $x^\alpha(\tau)$, from (2.32), we recall that

$$h_3^\alpha = \phi + \chi\xi\left(1-f^\alpha\right)\left|x_*^\alpha\right|\left(\frac{1}{|x_*^\alpha|+s_{th}}\right) \tag{2.40}$$

and note that since h_3^α is a function of x^α only, the rate equation (2.32) can be expressed as a function of x^α as follows:

$$\dot{x}^\alpha = h_3^\alpha\left(x^\alpha\right)\left(1-\frac{x^\alpha}{x_s}\text{sign}\left(\dot{\gamma}^\alpha\right)\right)\dot{\gamma^\alpha} \tag{2.41}$$

The equation can be analytically integrated from time t to time τ assuming that the $\dot{\gamma}^\alpha$ does not change sign during the interval $(t-\tau)$:

$$\int_{x^\alpha(t)}^{x^\alpha(\tau)} \frac{dx^\alpha}{h_3^\alpha\left(h_2^\alpha\left(x^\alpha\right)\right)\left(1-\frac{x^\alpha}{x_s}\right)\text{sign}\left(\dot{\gamma}^\alpha(t)\right)} = \int_{\gamma^\alpha(t)}^{\gamma^\alpha(\tau)} d\gamma^\alpha \tag{2.42}$$

Carrying out the integration and substitute in the value of $x^\alpha(t)$, we get

$$x^\alpha(\tau) = \left(\frac{ae-1}{be-d}\right) \tag{2.43}$$

where

$$a = \phi + \frac{1}{2}\chi\xi|x_*^\alpha| \tag{2.44}$$

$$b = -\frac{1}{2}\chi\xi\text{sign}(x_*^\alpha) \tag{2.45}$$

$$d = \frac{\text{sign}\left(\dot{\gamma^\alpha}(t)\right)}{x_s} \tag{2.46}$$

$$e = \left(\frac{1-d\cdot x^{\alpha}(t)}{a-b\cdot x^{\alpha}(t)}\right)\exp\left((b-a\cdot d)\Delta\gamma^{\alpha}\left(\tau^{\alpha}\left(\mathbf{T}^{*}(\tau)\right),s^{\alpha}(\tau),x^{\alpha}(\tau)\right)\right) \tag{2.47}$$

Equations (2.34), (2.36) and (2.43) are solved using a two level iteration procedure. The subscripts n and k, through this section, refer to the number of first level iterations, and second level iterations, respectively. The subscript p for $x_p^{\alpha}(\tau)$ refers to the $x^{\alpha}(\tau)$ obtained at p*th* trial of the whole iteration process.

In the first level of iteration, Eqn. 2.34 is solved for $\mathbf{T}^{*}(\tau)$ using Newton-type algorithm while keeping the estimates of $s^{\alpha}(\tau)$ and $x^{\alpha}(\tau)$ fixed. The Newton algorithm for $\mathbf{T}^{*}(\tau)$ is

$$\mathbf{T}^{*}_{n+1}(\tau) = \mathbf{T}^{*}_{n}(t) - \mathcal{J}_n^{-1}[G_n] \tag{2.48}$$

where

$$\mathcal{G}_n \equiv \mathbf{T}^{*}_{n}(\tau) - \mathbf{T}^{*^{tr}} + \sum_{\alpha}\Delta\gamma^{\alpha}\left(\tau^{\alpha}\left(\mathbf{T}^{*}_{n}(\tau)\right),s^{\alpha}_{k}(\tau),x^{\alpha}_{p}(\tau)\right)\mathbf{C}^{\alpha} \tag{2.49}$$

$$\mathcal{J}_n \equiv \mathcal{I} + \sum_{\alpha}\left\{\frac{\partial}{\partial\tau^{\alpha}}\Delta\gamma^{\alpha}\left(\tau^{\alpha}(\mathbf{T}^{*}_{n}(\tau)),s^{\alpha}_{k}(\tau),x^{\alpha}_{p}(\tau)\right)\right\}\mathbf{C}^{\alpha}\otimes\mathbf{S}^{\alpha}_{0} \tag{2.50}$$

As the iteration of the stress converges, we start the p*th* trial of the second level iteration by updating the value of $x_p^{\alpha}(\tau)$ using (2.43) with e in (2.47) estimated by $T^{*}_{n+1}(\tau)$, $s^{\alpha}_{k}(\tau)$ and $x^{\alpha}_{p-1}(\tau)$. After we obtain $x^{\alpha}_{p}(\tau)$ and accordingly, $h^{\alpha}_{2}(\tau)$, we are able to calculate an average value for h^{α}_{2} during t to τ

$$\bar{h}^{\alpha}_{2} = \frac{h^{\alpha}_{2}(t)+h^{\alpha}_{2}(\tau)}{2} \tag{2.51}$$

Using this averaged $\bar{h}^{\alpha}_{2}$, we start the second iteration by iterating the $s^{\alpha}(\tau)$ as:

$$\begin{aligned} s^{\alpha}_{k+1}(\tau) &= s^{\alpha}(t) + \sum_{\beta} h^{\alpha\beta}_{1}\left(s^{\beta}_{k}(\tau)\right)\left|\Delta\gamma^{\beta}\left(\tau^{\beta}\left(\mathbf{T}^{*}_{n+1}(\tau)\right),s^{\beta}_{k}(\tau),x^{\beta}_{p-1}(\tau)\right)\right| \\ &\quad -\bar{h}^{\alpha}_{2}\left(x^{\alpha}(t),x^{\alpha}_{p}(\tau)\right)\left|\Delta\gamma^{\alpha}\left(\tau^{\alpha}\left(\mathbf{T}^{*}_{n+1}(\tau)\right),s^{\alpha}_{k}(\tau),x^{\alpha}_{p-1}(\tau)\right)\right| \end{aligned} \tag{2.52}$$

In our calculation, the values of $\mathbf{T}^{*}(\tau)$ and $s^{\alpha}(\tau)$ are accepted if change in the absolute values are less than $10^{-3}s_0$ for $\mathbf{T}^{*}(\tau)$ and $10^{-4}s_0$ for $s^{\alpha}(\tau)$. Otherwise, this new estimates of $s^{\alpha}(\tau)$ and $x^{\alpha}(\tau)$ are used to restart the iteration. Since we use an exact analytic integration to calculate $x^{\alpha}(\tau)$ from t to τ, it only need to be calculated once at the beginning of each second level iteration and its convergence is implied by the convergence of $\mathbf{T}^{*}(\tau)$ and $s^{\alpha}(\tau)$.

The remaining task for time-integration scheme is essentially the same as the polycrystal model by Kalidindi, Bronkhorst and Anand (1991).

In the next chapter, we verify our model by comparing a set of experimental data to simulation results based on experimentally obtained parameters. We will show that the validity of the model is supported by a good match between the simulation and experimental results.

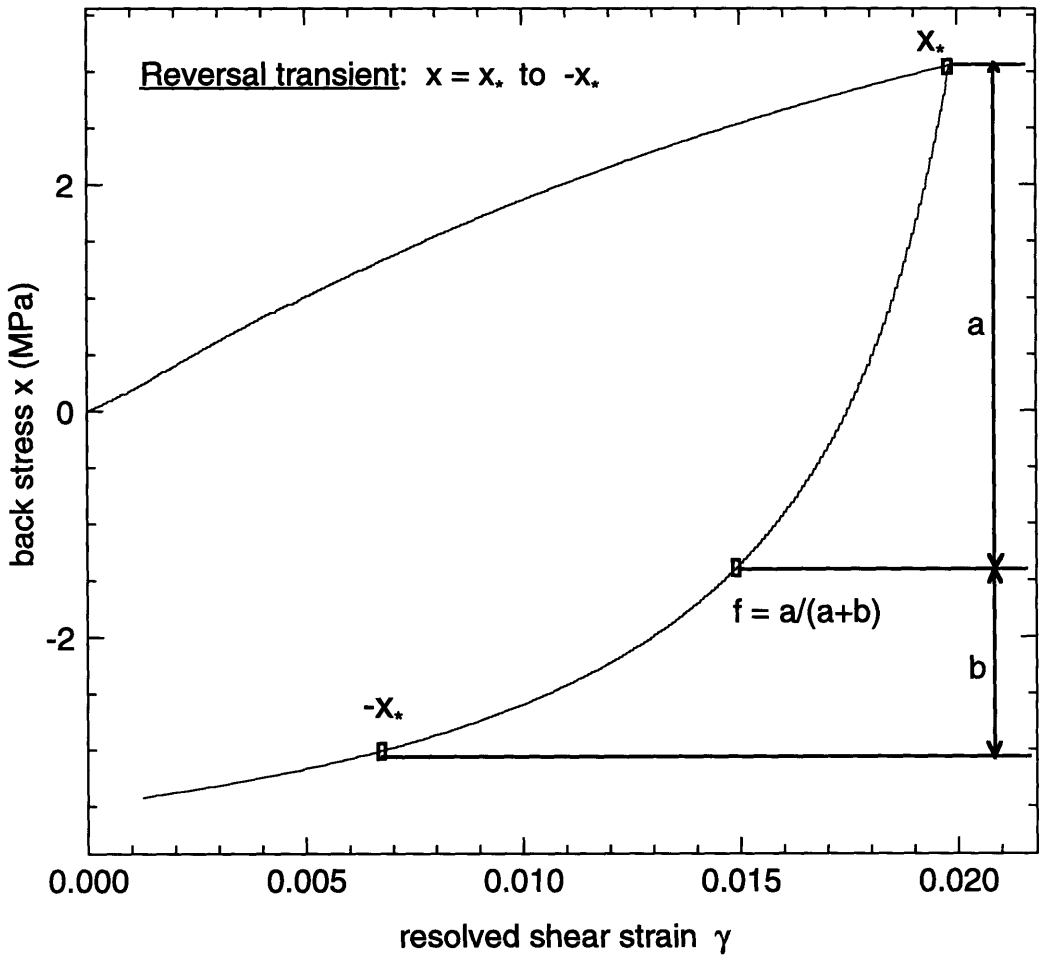

Figure 2-1: Definition of "reversal transient" and related parameters x_*, and fraction f.

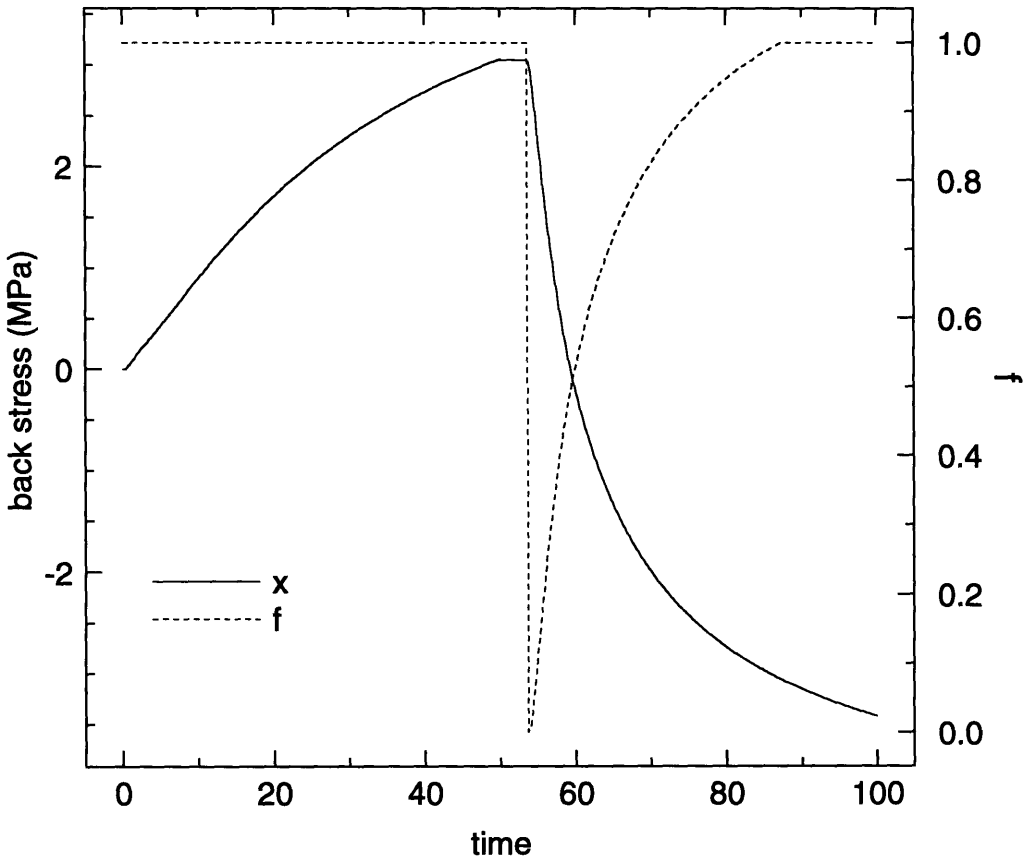

Figure 2-2: Evolution of f, and x versus time in a single reversal simulation. At the beginning of the reversal (time ≈ 50), x_* is set to be equal to x and f to be zero. During the reversal, f increase to 1 while x keeps decreasing.

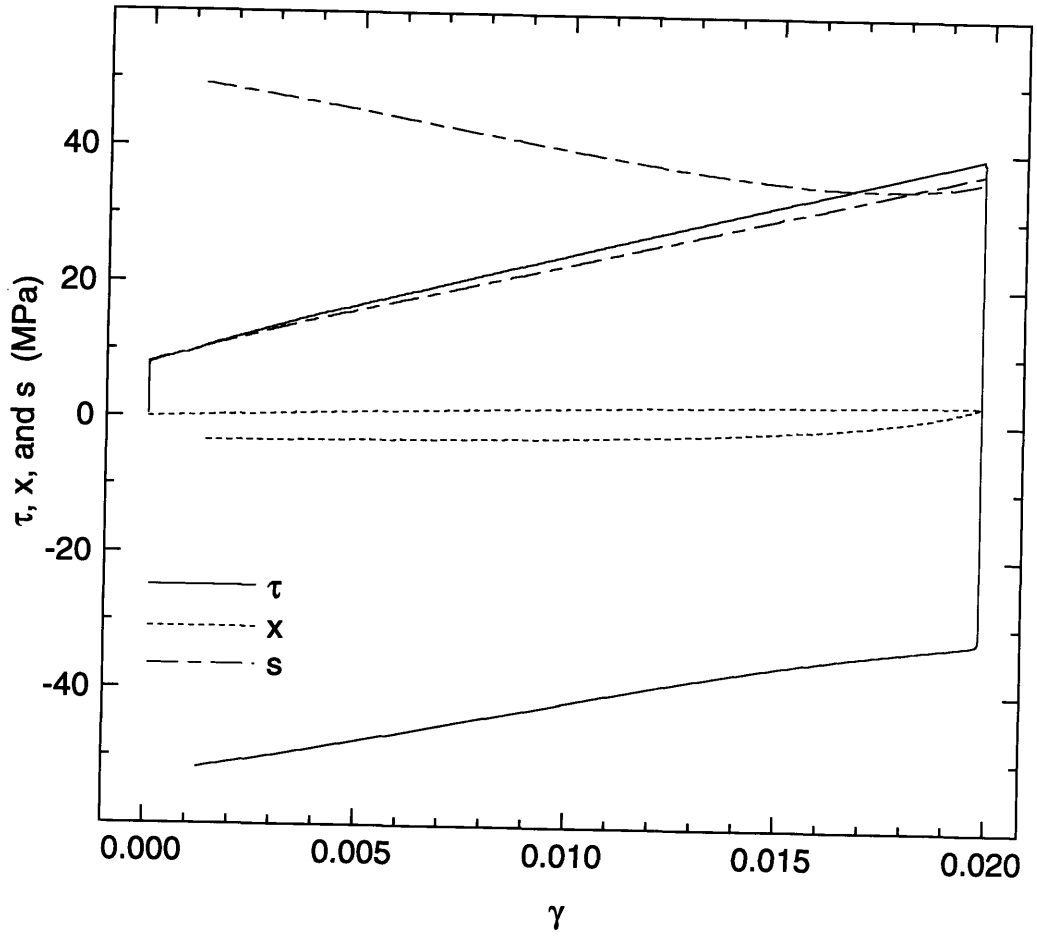

Figure 2-3: Evolution for resolved shear stress (τ), s and x versus resolved shear strain in simulation

Chapter 3

Verification of the Constitutive Model

3.1 Experimental Apparatus

The experiments were conducted on a stiff servo-hydraulic testing system (Fig. 3-1). The testing system features a high stiffness biaxial test frame equipped with MTS series 646 hydraulic collet grips, and the load capacity is 50,000 lbs (222 kN) / 20,000 inch-lbs (2260 N-m). The machine is controlled on both channels with an analog controller. Acquisition of data is performed with the software package LabTech Notebook through a Keithley Series 500 hardware interface installed on an Intel 486/50 personal computer. Prior to the tests, the load train is carefully aligned by adjusting four alignment screws on the top of the load train to make sure that the misalignment is less than 0.0005" circumferentially.

High conductivity oxygen free copper is chosen as the candidate material for all testing. Round tension-compression and tension-torsion specimens are machined from as-received 0.5" and 2" diameter rods. The dimensions of the uniaxial test sample and axial-torsional sample are shown in Fig. 3-2 and Figs. 3-3, 3-4, respectively. Prior to the tests, all samples were annealed in an Argon-filled furnace, to remove any residual stress or pre-textures. The samples were heated up to 800^oC in two hours, soaked for one hour and then furnace cooled to room temperature in nine hours. After annealing, photo-micrographs of the polished-etched sample were taken (Figs. 3-5, 3-6). The grains are equiaxed and their average size is about 60 μm. The annealed material shows a relatively low yield strength of 25 MPa.

The uniaxial tension/compression cyclic test were performed under strain and load control mode to precisely characterize the strain in the gage section. For these tests, the strain data are collected through an extensometer with maximum range of ± 0.1 inch.

Lacking a biaxial extensometer, the biaxial cyclic test were performed under position control. However, a strain gage rosette was carefully aligned and glued on the surface of the gage section of the specimen to provide a measurement of the cyclic strain in the gage section. During the test, displacement readings from LVDT and RVDT are collected together with the readings from the strain gages. These two data are compared to check the accuracy of LVDT/RVDT readings in providing accurate measures of gage section strains. Noting that the relative importance of the shoulder sections depends on their length, as compared to gage length, it is found that the deformation of the shoulder sections plays a less important role for the tests performed on the long gage length torsional samples. The strain amplitude is almost uniform through the test. For the short gage section samples, the deformation in the shoulder section is relatively larger.

3.2 Material Parameter Evaluation

In order to perform numerical simulations using the present model, we need to estimate the material parameters. The parameters in the present model include elastic modulus C_{11}, C_{12}, C_{44}, rate sensitivity m, plastic resistance parameters s_0, s_s, x_s, s_{th}, and hardening parameters a, η, ξ, ϕ, χ, and q. In this section, a methodology for determining the material parameters is given and applied to the material under consideration.

The experiments that were required to determine the parameters consisted of the uniaxial monotonic test and the uniaxial cyclic tests, and the steps used to determine the material parameters are as follows:

1. Obtain C_{11}, C_{12}, and C_{44} from handbooks.

Elastic moduli C_{11}, C_{12}, and C_{44} should be obtained from ultrasonic testing and for copper are available in handbooks (e.g. Simmons and Wang, 1971).

2. Determine m and q.

The value of rate sensitivity m for OFHC copper is obtained by fitting a uniaxial strain rate jump test performed by Bronkhorst (1991) with $\dot{\gamma}_0$ set to be equal to macroscopic strain rate. Characterization of latent hardening is perhaps the most difficult part of the

constitutive model. Here we simply take the latent hardening factor q as 1.4.

3. Determine ϕ and x_s from uniaxial single reverse test.

Several symmetric strain cycling tests with different strain amplitudes were performed in order to determine the back stress versus strain curve, by utilizing the first reversal data. We define the level of back stress at each strain amplitude to be half of the difference of corresponding forward flow stress and reverse 0.2% offset yield stress. For polycrystal materials, the averaged resolved shear stress is about one-third of the macroscopic tensile stress. Using this relation, we can approximate the resolved-shear-stress/strain curve. On the other hand, because during a monotonic deformation the term contains χ in the expression for h_3 is zero, h_3 equals ϕ and we can integrate Eqn. 2.32

$$\int_0^x \frac{dx}{\phi\left(1-\frac{x}{x_s}\right)} = \int_0^\gamma d\gamma \tag{3.1}$$

and get the back stress- strain relationship

$$-\frac{x_s}{\phi}\ln\left(1-\frac{x}{x_s}\right) = \gamma \tag{3.2}$$

The initial guess of x_s and ϕ is obtained by nonlinear fitting such equation to the back stress-strain $(x-\gamma)$ curve. These values are then checked and fine-tuned using a finite element simulation of a monotonic test. Fig. 3-7 shows the results from fitting the experiment data of OFHC copper.

4. Determine a, η, s_0, s_s, and q from uniaxial monotonic test.

After the back stress-strain curve are determined, we can exclude its contribution from the total resistance (flow stress) and get the isotropic resistance-strain data. Since h_2 is zero during a monotonic test, the deformation resistance-strain relation (2.5) is again integratable without considering latent hardening effect.

$$\int_{s_0}^{s} \frac{ds}{\eta\left(1-\frac{s}{s_s}\right)^a} = \int_0^\gamma d\gamma \tag{3.3}$$

then

$$\frac{s_s}{\eta(a-1)}\left(1-\frac{s}{s_s}\right)^{1-a}\Bigg|_{s_0}^{s} = \gamma \tag{3.4}$$

Therefore, a first guess of s_0, s_s ,a and η could be obtained using similar procedures as for

x_s and ϕ from nonlinear curve fitting (3.4) to the resistance-strain data . From experience it is found that we need to reduce η by about 5 times and adjust a a little bit after including the latent hardening relationship for s. After a few trials, a proper set of a, η, s_o, and s_s will be obtained to give a reasonable fit the monotonic stress strain response (Fig. 3-7).

5. Determine χ and ξ from fitting the uniaxial cyclic tests.

After all other parameters are determined, ξ and χ is obtained by trial and error to get a best fit of at least two stress-strain curve from the uniaxial cyclic tests data. The general rule for adjusting these two parameters is: increase χ to increase the initial slope of each reversal and saturation stress level; increase ξ to increase the permanent softening and reduce the saturation stress level. Since there is a competing effect between ξ and χ, it requires a few trials to get these two parameters.

The complete set of parameters for Copper obtained is listed in Table 3.1 below. Where a, m, and q are dimensionless and the rest have dimension of MPa.

C_{11}	C_{22}	C_{44}	η	ξ	ϕ	χ
150.E+3	110.E+3	75.E+3	325.0	138.0	448.0	1.5625
s_0	s_s	x_s	a	m	q	
8.0	133.0	5.0	2.1	0.012	1.4	

Table 3.1: Material parameters for annealed OFHC copper

3.3 Uniaxial Symmetric Strain Cycling

To verify our cyclic crystal plasticity model, we check its performance by matching cyclic tests with equal positive and negative cycling strain range–the symmetric strain cycling. The model should be able to capture the whole deformation process for each strain range, up to the saturation level. These tests are also the primary tests for determining the set of material parameters, as indicated in the previous section.

Five tests, with strain range of 0.3% to 3%, are performed and the tests data and simulations are shown in Fig. 3-8 to 3-12. The model are able to closely match the stress-strain response up to saturation. There is some discrepancy in the vicinity of each reversal; the simulation shows a little sharper turn in this regime.

One important feature of the model worth pointing out is that the saturation level is determined by the balance of hardening (due to h_1) and softening (due to h_2) of deformation resistance s. As the cycling process advances, the hardening rate decreases, but the softening rate increases due to the augmentation of back stress. At the stress level where these two competing effect balance and no more further hardening is achieved in each half cycle, the material reaches saturation.

Such softening phenomena in cyclic loading is supported by the experimental work of Hasegawa *et al.* (1975) and Christodoulou, *et al.* (1986) as indicated in Chap. 1. The effect of back flow is similar to annealing in the way that both of them reduce the deformation resistance, or equivalently, the density of forest dislocations. Kocks, Hasegawa and Scattergood (1980) interpret such softening as an stress induced dynamic recovery which is effective only on unstable cell components.

We could also imagine the whole reversal transient in terms of dislocation interaction mechanisms proposed by Orowan. The annihilation could be inferred by the backward motion of piled-up dislocations from forest dislocations or three dimensional networks, when the resolved shear stress changes sign. As these unstable dislocations move in the "backward" direction, reducing the density of dislocation around the entanglement of dislocation, the back stress is reduced and the deformation resistance appears lower (at the beginning of the stress reversal). When deformation continues in the backward direction, another back stress field opposing the continuous shearing will be built up. Besides, since dislocation cells are polarized as suggested by Kocks (1979), it is very possible that these backward moving dislocations will encounter and cancel some dislocations of the opposite sign in the blocking dislocation structures. These effects justify the physical background for the h_2 term in our model, and point out a possible qualitative connection between our internal variables and evolution equation for our micro-structural elements.

After verifing the current model by comparing its predictions to symmetric strain cycling data, in the next chapter we try to predict other cyclic loading responses.

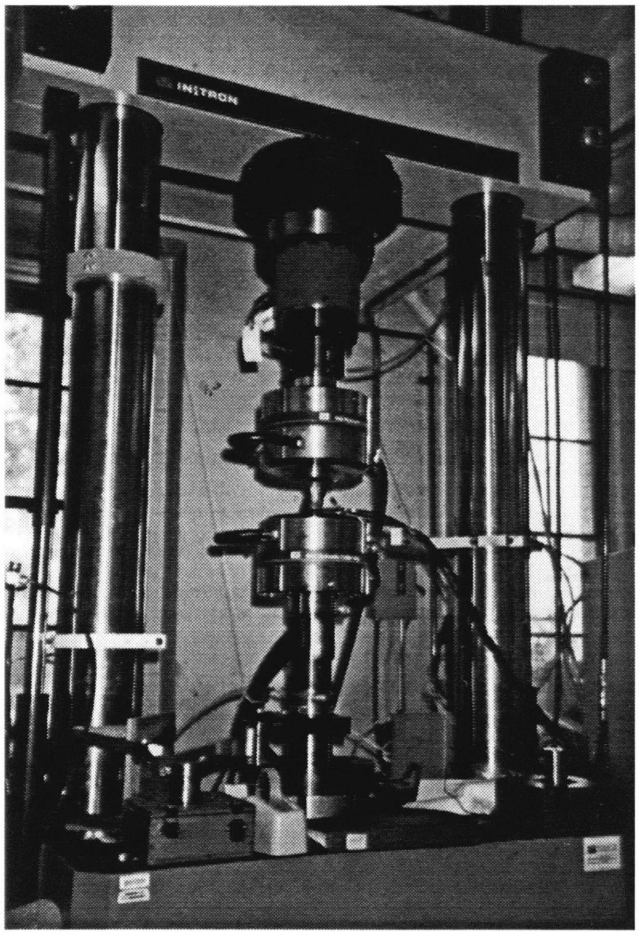

Figure 3-1: Instron biaxial testing frame.

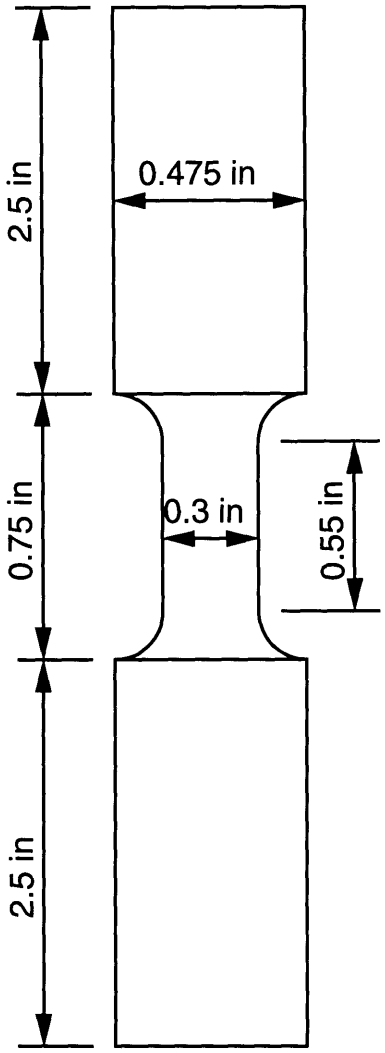

Figure 3-2: Tension-compression cyclic test sample.

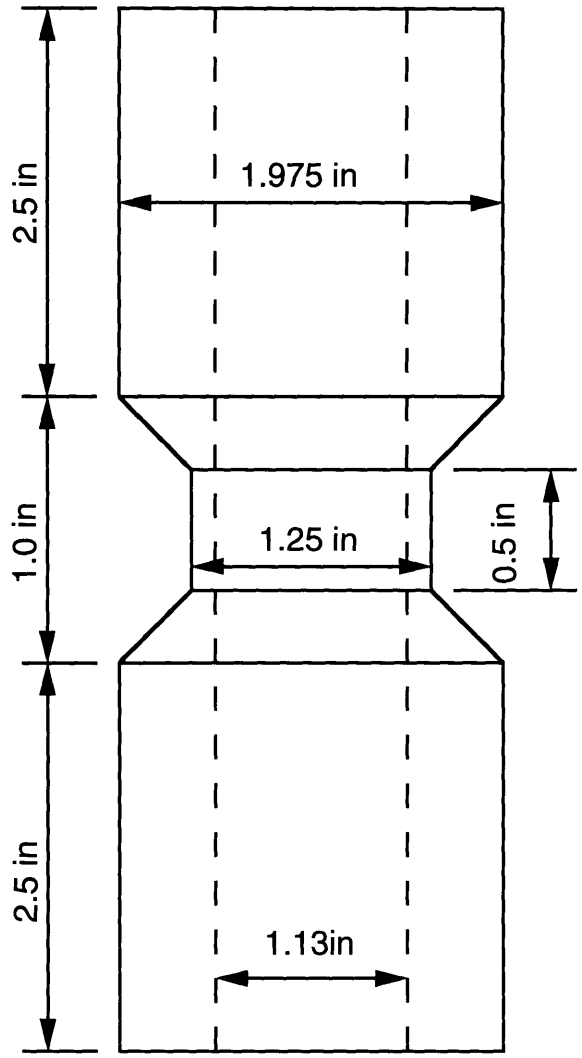

Figure 3-3: Axial-torsional cyclic test sample, short gage length.

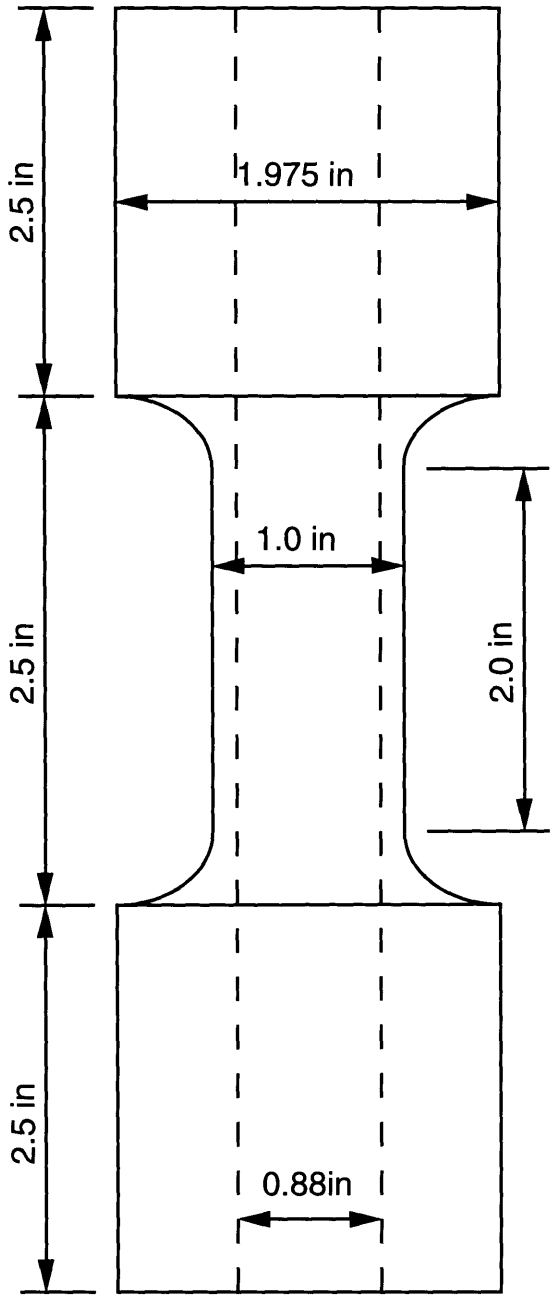

Figure 3-4: Axial-torsional cyclic test sample, long gage length.

Figure 3-5: Photo-micrograph of annealed OFHC copper taken perpendicular to the rod axis. (×1600)

Figure 3-6: Photo-micrograph of annealed OFHC copper taken parallel to the rod axis. ($\times$1600)

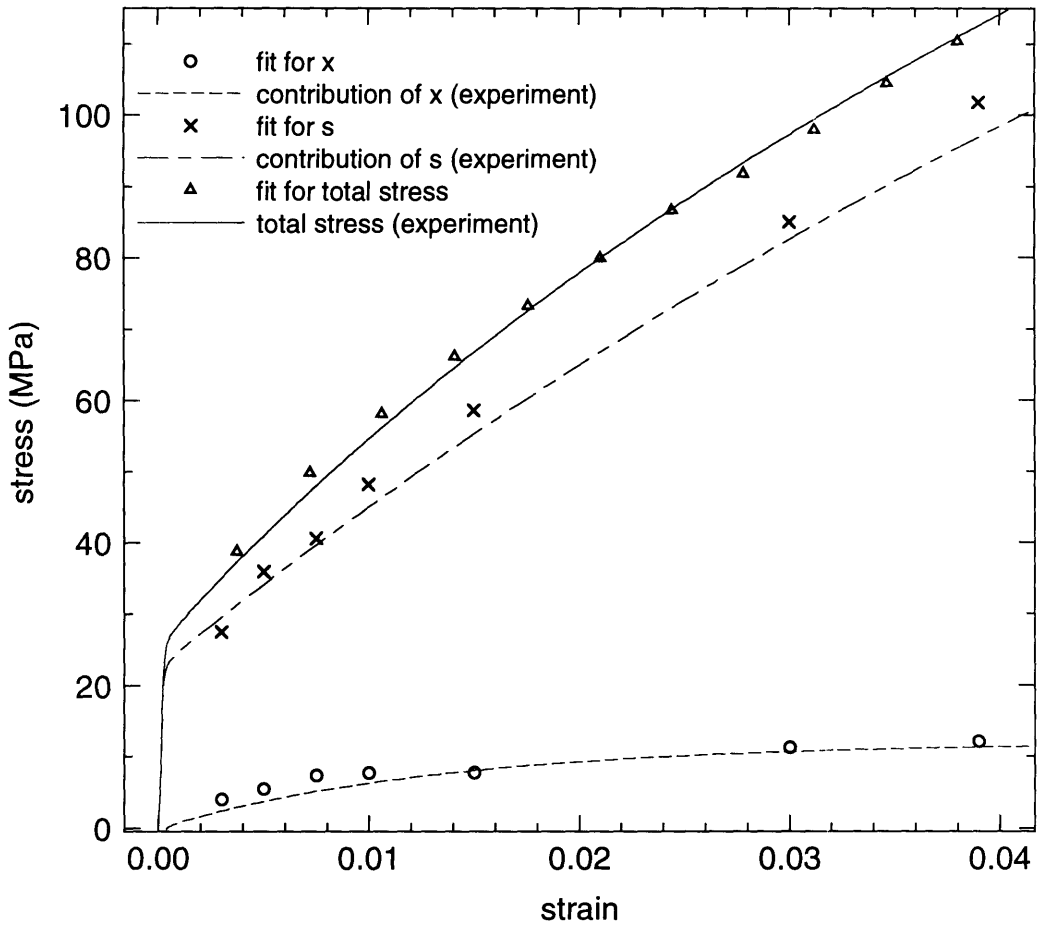

Figure 3-7: Fit of x, and s for OFHC copper.

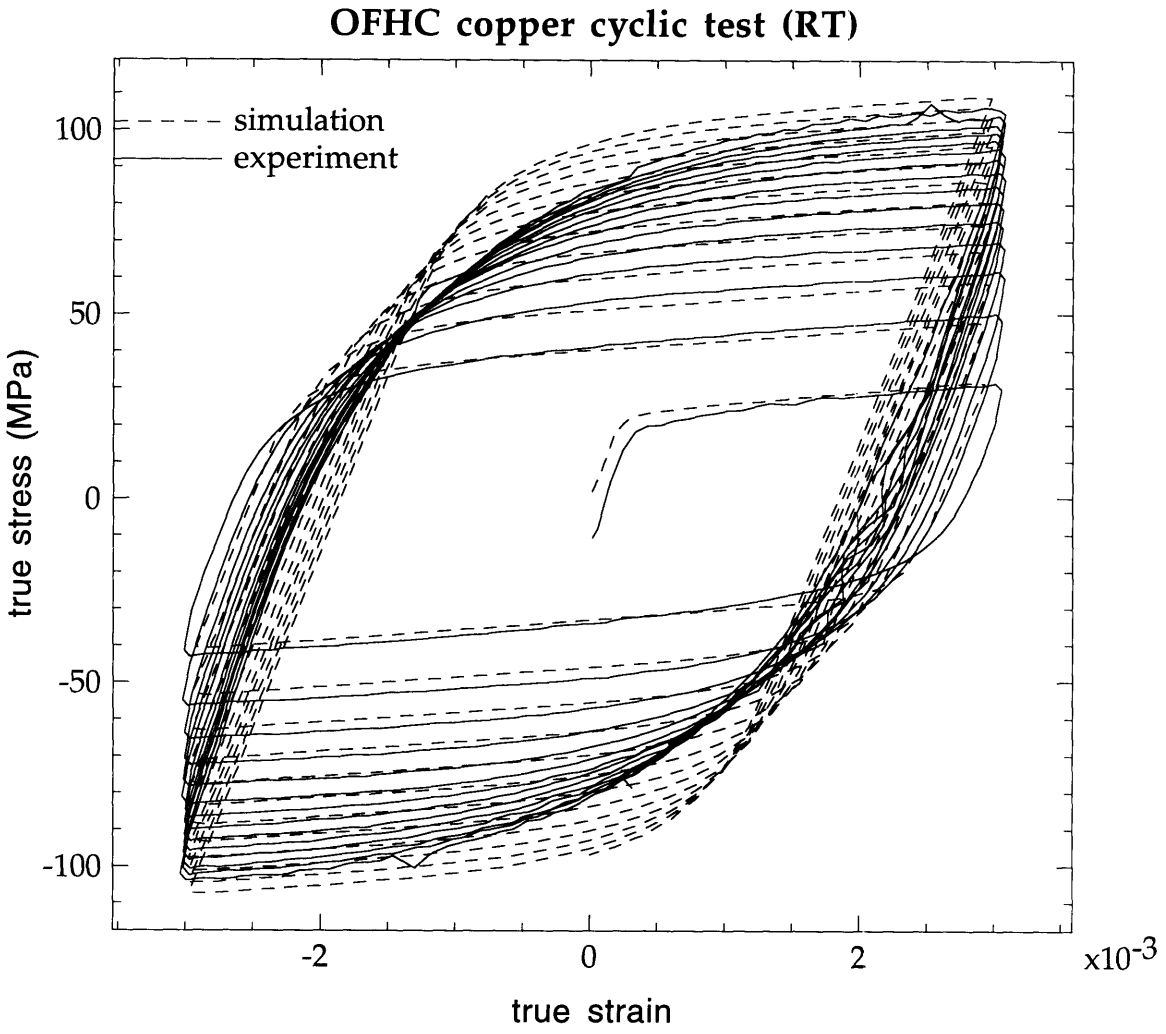

Figure 3-8: Symmetric strain cycling test, $\epsilon_a = 0.3\%$.

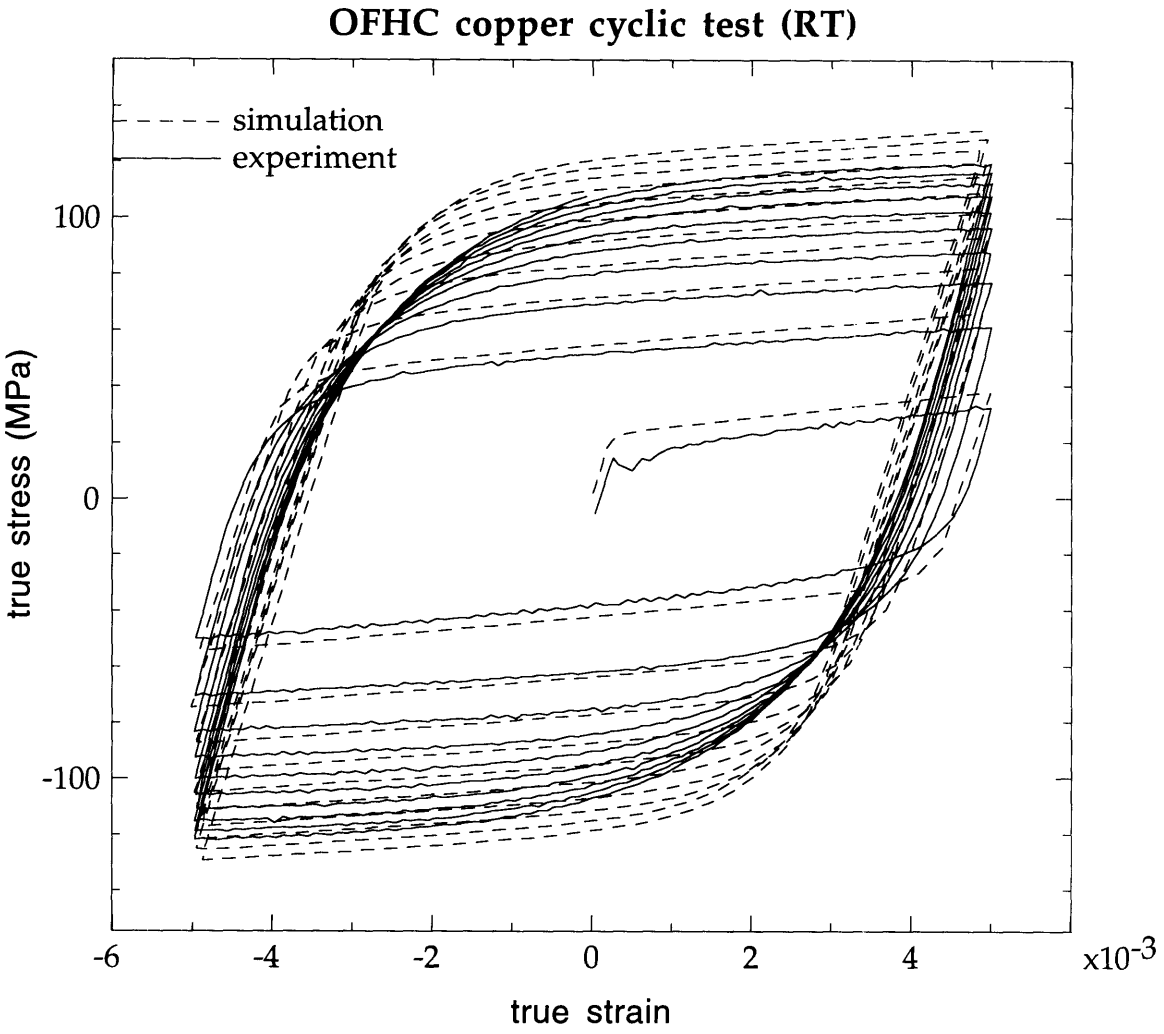

Figure 3-9: Symmetric strain cycling test, $\epsilon_a = 0.5\%$.

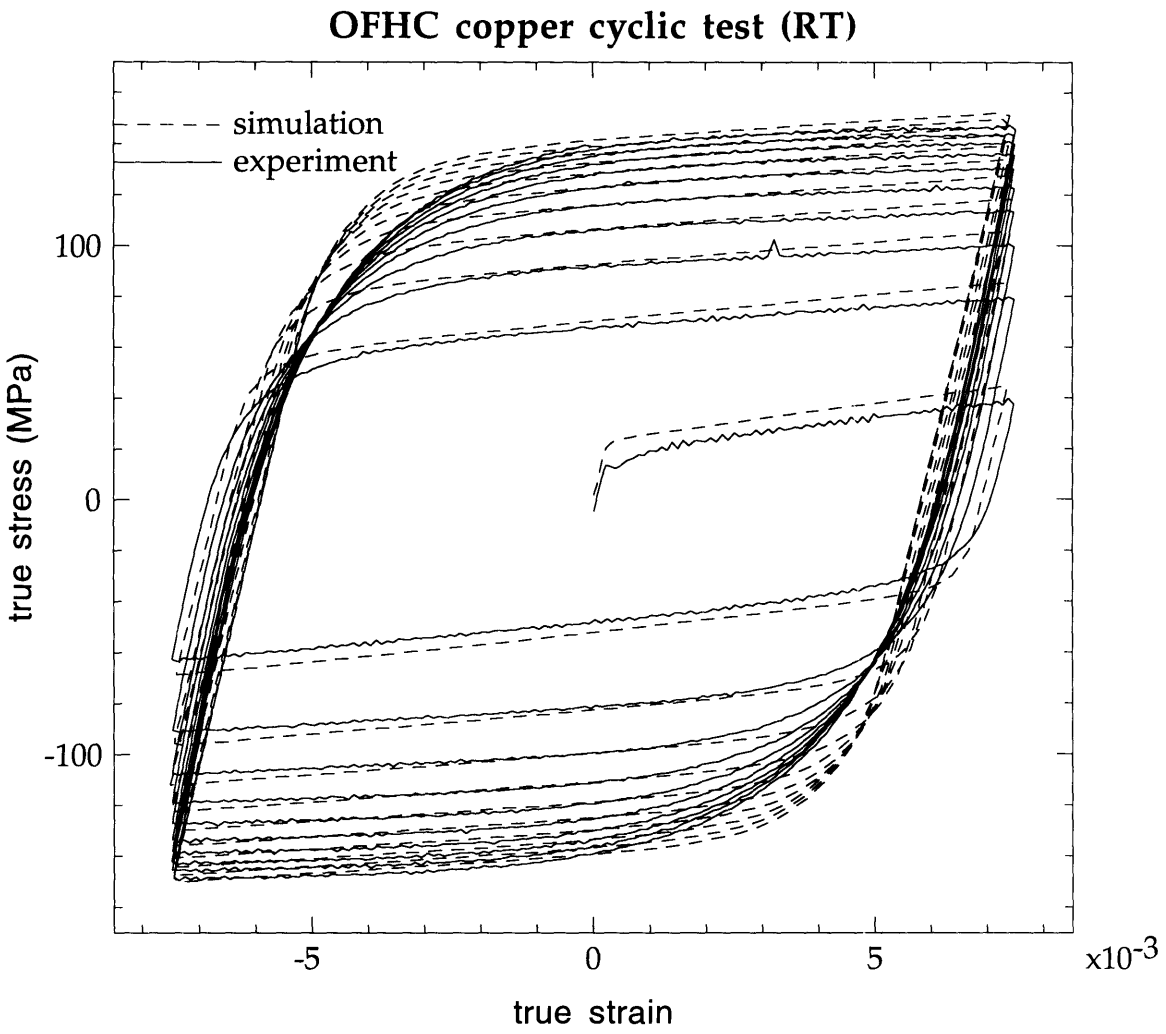

Figure 3-10: Symmetric strain cycling test, $\epsilon_a = 0.75\%$.

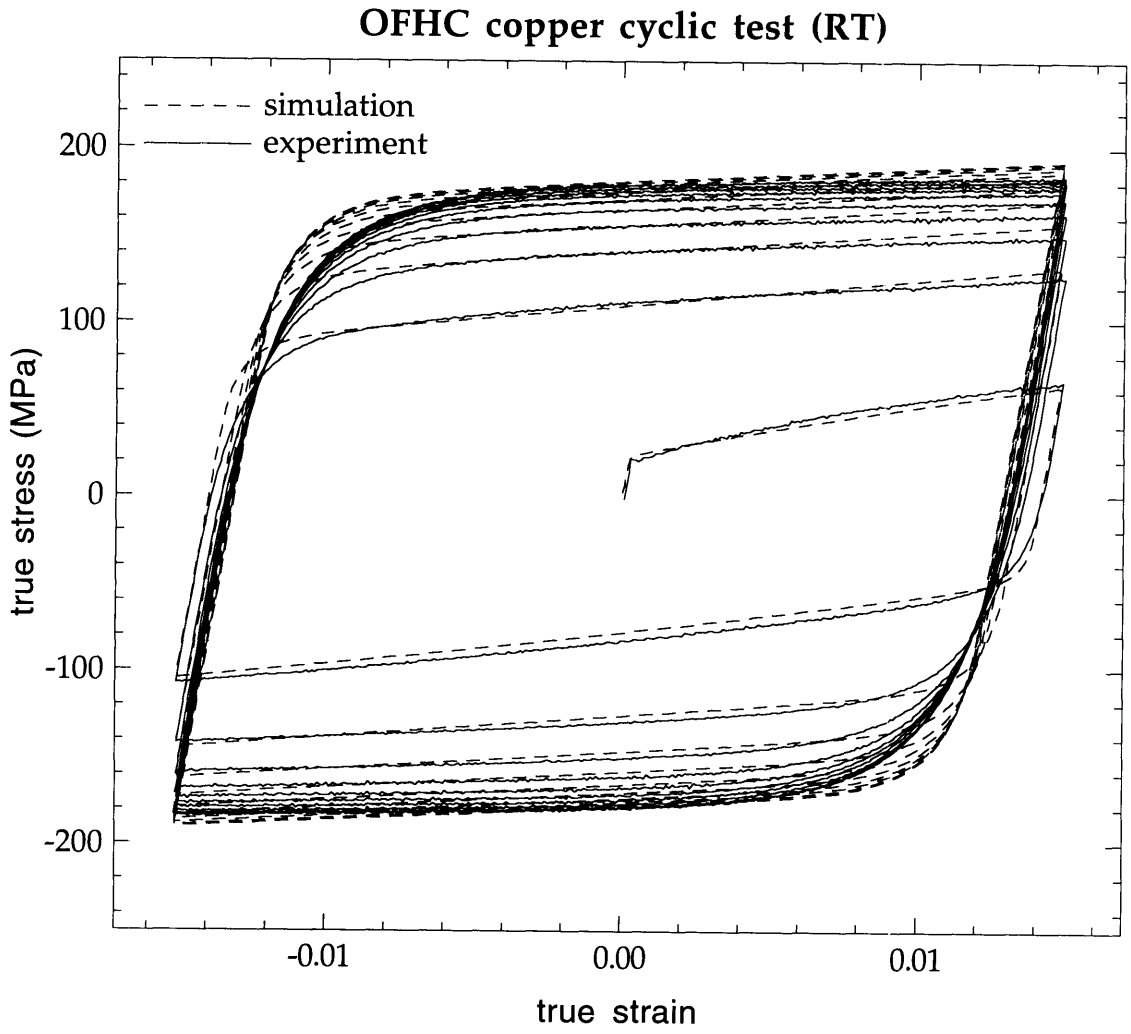

Figure 3-11: Symmetric strain cycling test, $\epsilon_a = 1.5\%$.

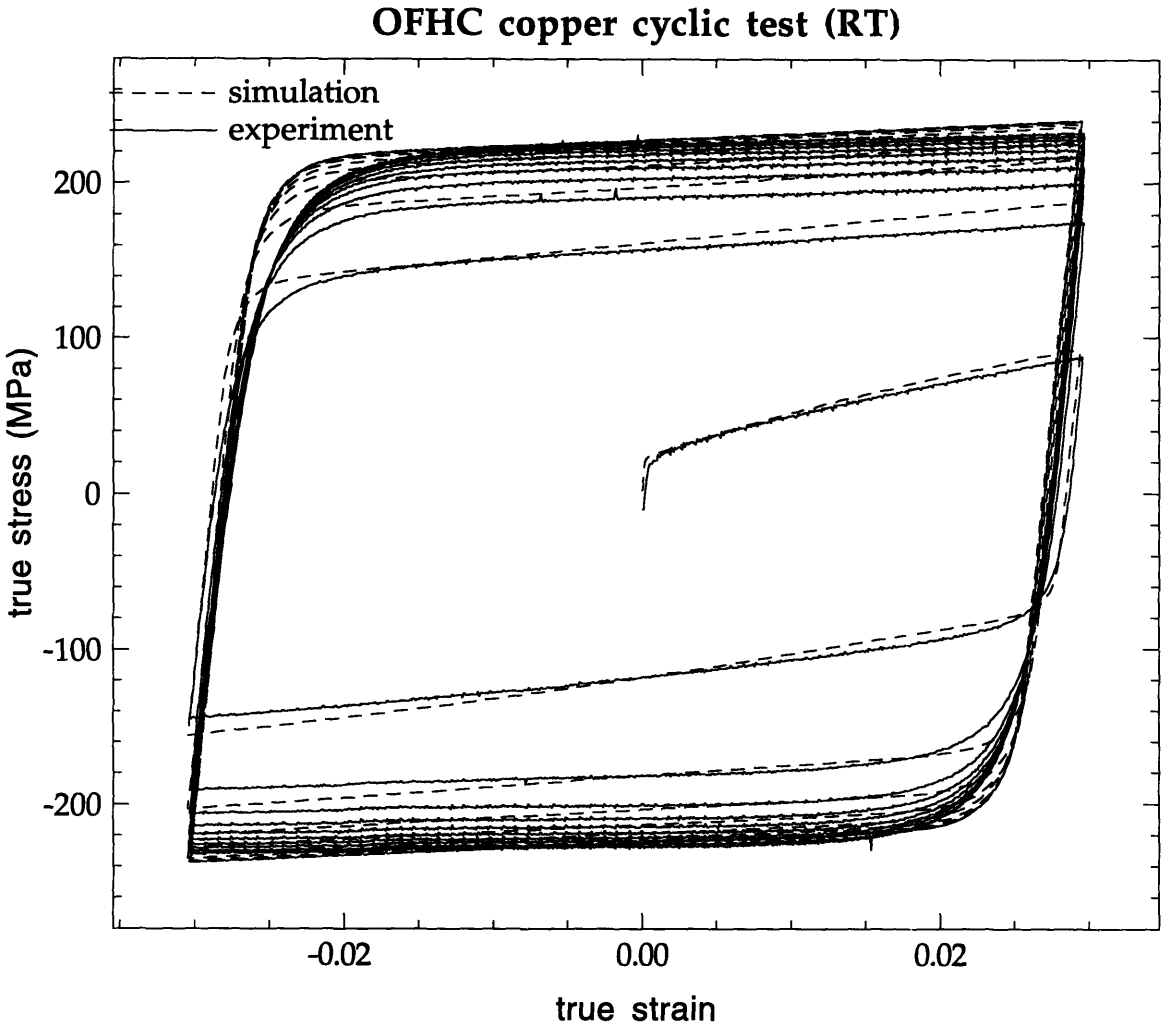

Figure 3-12: Symmetric strain cycling test, $\epsilon_a = 3\%$.

Chapter 4

Predictions

After we obtain the material parameters we are able to predict the material's stress-strain response under different loading conditions. In order to evaluate the predictive capability, it is imperative to choose loading conditions which are different and more complex than the experiments from which the material parameters were determined. In the current study, we try to predict the stress-strain response for unsymmetric axial strain and unsymmetric axial stress controlled cycling. We also examine a ninety degree out of phase non-proportional tension-torsion cycling, and a proportional "butterfly" straining pattern in tension-torsion. The results are presented in the following sections.

4.1 Unsymmetric Axial Strain Cycling

Instead of performing cyclic test with equal positive and negative strain range, we performed strain controlled cyclic test within two unsymmetric strain bounds. For an annealed material undergoing small unsymmetric strain the material strain hardens during unsymmetric strain, and the mean stress approaches zero at saturation.

The prediction accompanied by the experimental data for a test with strain range 1%±0.75% is shown in the Fig. 4-1. The predictions of the model are in good accord with experiment. If we compare the results to the symmetric strain cycling test with equal strain amplitude (Fig. 3-10), we find that the flow stress starts higher for the unsymmetric cycling but the saturation level for these two tests are about equal. In other words, the contribution of the initial strain offset to the hardening gradually disappears as the number of cycles increases.

4.2 Unsymmetric Uniaxial Stress Cycling

Materials experiencing unsymmetric cyclic stress undergo cyclic creep. If the material softens substantially, then the ratcheting process will accelerate, leading to an unstable behavior with increasing creep strain for each cycle. A catastrophic failure of the material usually occurs after a large number of cycles, and the use of such a material in applications under fatigue loading is considered inappropriate. On the contrary, a strain-hardening material is relatively more stable, and the creep strain in each cycle gradually decreases to zero, and the ratcheting ceases. These observations are demonstrated by the schematic drawing show in Fig. 4-2. The fully-annealed copper of the current study belongs to the latter case, and we expect little ratcheting in this material.

The unsymmetric stress cycling test, or ratcheting test was also performed on the OFHC annealed copper[1], with the specimen cycled between stress limits of 50 MPa in tension and 40 MPa in compression. This specimen was not from the same heat-treated bunch as for the strain-controlled experiments, and the yield strength is about 9 MPa higher. To account for the difference, in the simulation, we needed to adjust the parameter s_0 by 3 MPa to account for the difference in the yield strength. All other parameters were unchanged. The prediction and experiment of this ratcheting test is shown in Figs. 4-3 and 4-4. We see that the prediction is quite close to the experiment. The predicted strain level and shape of the saturation loop resemble the test results closely.

Due to the incompatibility between grains as materials go through an elastic-plastic transition, the small strain range cyclic modeling has been a difficult problem to deal with. Our model does show good predictability for the uniaxial cyclic tests performed in the small strain range. For either strain or stress controlled test, the model capture the response from yielding all the way to saturation. Moreover, the smooth elastic-plastic transition is also captured with reasonable accuracy.

In the next section, we move on to a more challenging objective – predicting small strain biaxial cycling, to better evaluate the predictive capability of the model.

[1]One thing to remember while comparing the stress controlled test data to the strain controlled ones is, the strain rate is not constant in order to keep a constant stress rate, and vise versa. Therefore, for a rate-dependent material, the response of these two tests could be slightly different. However, knowing that the copper is quite rate-insensitive at room temperature (rate sensitivity $m = 0.012$, see Table 3.1), we expect to get similar monotonic curves from strain or stress controlled tests.

4.3 Axial-Torsional Cycling

4.3.1 90^o out-of-phase cycling

For multiaxial tests, in the classical literature based on isotropic plasticity, it is common to use equivalent stress and strain measures to evaluate tests results and compare them with those obtained from uniaxial tests. The definition of equivalent stress is

$$\bar{\sigma} \equiv \sqrt{\frac{3}{2}(\mathbf{T}' \cdot \mathbf{T}')} \tag{4.1}$$

where $\mathbf{T}'$ is the deviatoric stress. The definition of equivalent strain is

$$\bar{\epsilon} \equiv \sqrt{\frac{2}{3}(\boldsymbol{\epsilon}' \cdot \boldsymbol{\epsilon}')} \tag{4.2}$$

where the $\boldsymbol{\epsilon}'$ is the deviatoric strain. In uniaxial tensile/compressive loading, the equivalent stress/strain measures reduce to usual uniaxial stress/strain measures. However, in pure shear, the equivalent stress will be $\sqrt{3}$ times the shear stress, and the equivalent strain is shear strain divided by $\sqrt{3}$.

One of the biaxial experiments cited frequently in the literature as a basic test of non-proportional cyclic plasticity, is the axial-torsional 90^o out-of-phase cyclic test. This involves radial loading in either the tension or shear direction to a certain prestrain, then cycling by following a circular trajectory in the strain space keeping the equivalent strain amplitude constant. That is, the normal and shear strain are related by

$$\epsilon = \bar{\epsilon}_a \sin(2\pi\omega t) \tag{4.3}$$

$$\gamma = \sqrt{3}\,\bar{\epsilon}_a \cos(2\pi\omega t) \tag{4.4}$$

where $\bar{\epsilon}_a$ is a constant equivalent strain amplitude and ω is the cyclic frequency. Generally speaking, such 90^o out-of-phase cycling shows maximum "extra hardening" and leads to highest saturation stress levels as compared to uniaxial cycling and other biaxial cycling with the same equivalent strain amplitude. On the contrary, proportional cycling (no phase lag between shear strain and normal strain) will show the same response in the equivalent stress-strain space.

Lacking a biaxial extensometer, several 90^o out-of-phase cycling tests were performed

under position control with different displacement amplitudes. Because the material strain-hardens a lot, the radius and the shoulder sections of the axial-torsional specimens gradually plastically deform at higher stress level. This end effect makes the actual strain inside the gage section hard to identify from displacements and rotations measured by LVDT/RVDT mounted at the end of the load-train. To better characterize the strain in the gage section, a strain gage rosette was carefully aligned and glued on the surface of the gage section of the specimen to provide a measure of the cyclic strain in the gage section. During the test, displacement readings from the strain gages are collected together with those from LVDT/RVDT. This method also has its drawbacks considering the hysteresis effect of the strain gage in cyclic deformation (it is about 15% at maximum), and possible non-uniform of strain around the gage section. Taking advantage of both strain measuring methods, the strain data used in the simulation is approximated by comparing the LVDT/RVDT strain for the whole process to the *first* cycle of strain obtained from strain gage glued on one side of the gage section.

The results for both simulation and experiment of two test with $\bar{\epsilon}_a = 1\%$ are shown in Fig. 4-5 and 4-6. Compromising between the speed and accuracy, the simulations were performed using four 3D eight-noded elements.[2] In the simulations, we fix the bottom surface in the loading directions, and pulling and shearing the the top surface nodes together at the same time. Taylor's assumption is applied by averaging the response of a set of 50 crystal orientations at each integration point. As we see from the figures, the simulation is reasonably close to the experiment for the first three cycles, then it under-predicts the data at saturation. The mismatch is possibly due to the uncertainty of strain data. Even through the prediction is not as good as in the uniaxial case, the model still captures the main features of the test such as a spiraling outward stress trajectory, and a higher saturation level compared to monotonic cycling. (Fig. 4-8) Another simulation is also performed to be compared with a test with $\bar{\epsilon}_a = 0.75\%$ (Fig. 4-7). The discrepancy at higher stress level is similar to the ones with $\bar{\epsilon}_a = 1\%$.

A possible reason for the under-prediction of the saturation loop lies in the model itself.

[2] A one element simulation is faster; however, the $\tau - \sigma$ curve obtained is slightly faceted, possibly due to improper finite element procedures from overly constrained boundary conditions (the exact reason is unclear). Another full geometry simulation was also performed with 400 elements. In this case, while giving out a rather smooth stress trajectory, the job takes fours days on a HP 735 with only one random orientation assigned at each integration point.

Assuming the simulation strain input is the same as the experimental strain input, from the under-prediction at higher number of cycles we conclude that a smaller softening (or a stronger hardening) in 90^o out-of-phase biaxial cycling is required for the model to capture the higher stress levels obtained in the experiments. From the way the hardening rule is formulated (Eqn. 2.5), we will get the same softening effect for either proportional or non-proportional cycling because there is no interaction of softening between each slip system. Nevertheless, a small increase of hardening in non-proportional cycling is obtained in the simulation (Fig. 4-8) through the latent hardening relationship (q=1.4) because the latently hardened slip systems have a higher potential of becoming active in a non-proportional cyclic deformation process. In a back and forth (proportional) small strain cyclic loading, the primary slip systems are not expected to change, and the extra 40% hardening effect through latent hardening only affect the inactive slip system and will have no contribution to the macroscopic response.

From Fig. 4-5, considering the mismatch is about 20MPa at maximum, only 10% of the saturation stress, we believe our model is reasonably adequate to predict the 90^o out-of-phase cycling and there is no overwhelming need to further complicate the model and calculation procedure. We should keep in mind that although such latent hardening interactions might improve the accuracy of the model further, there will be a penalty of substantial increase of calculation time.

Although a 90^o out-of-phase cycling is an extreme case for maximum hardening among all cyclic process of the same equivalent strain, the phase lag is kept constant along the deforming process. A "butterfly" cyclic test in which the phase lag is constantly changing is considered more general for checking the validity of the model to be applied to random cyclic loading condition. We examine this case in the next section.

4.3.2 Butterfly strain cyclic test

A "butterfly" strain cyclic test involves a biaxial cyclic test with the following strain input:

$$\epsilon = \bar{\epsilon}_a \sin(4\pi\omega t) \tag{4.5}$$

$$\gamma = \sqrt{3}\bar{\epsilon}_a \sin(2\pi\omega t) \tag{4.6}$$

The name of this test comes from the geometric shape of the trajectory of strain in the (ϵ, γ) strain space — a butterfly — as shown in figure 4-9. It is essentially a non-proportional cyclic test with a variable phase lag between normal and shear strain. In each cycle, the phase lag varies from 0^o to 90^o, down to -90^o, then back to 0^o. It is a challenging task for a model to correctly predict the results of such an experiment.

A "butterfly" cyclic test was performed on the OFHC annealed copper using the long gage section thin-walled tube under position control. The strain in the gage section was estimated in the same way as that in the 90^o out-of-phase experiment, that is, by estimating from both strain gage and LVDT/RVDT data. We ran 10 such strain cycles, and the specimen started to show some buckling after the fifth cycle; therefore, only the data from the first five cycles are used for comparison with the simulation results.

As shown in the Fig. 4-10, a good match between the experiment and prediction is obtained from the current model. The prediction is from a four elements simulation as described in the previous section and the first five cycles are quantitatively well predicted by the simulation. This is a very pleasing result which demonstrates the robustness of the model in predicting complicated multiaxial cyclic stress-strain response.

4.4 Further predictions

In this section, we present predictions of results of tests not conducted under the current research program. The general idea is to check if we can predict the key feature of the test demonstrated by other workers studying complicated deformation path changes in metals. The tests includes, large strain reversal torsion by Teodosiu *et al.*(1992), and a strain path change experiment by Rauch and Schmitt(1989).

4.4.1 Large strain torsion reversal test

Although the focus of the current study is on small strain cyclic test. The model is completely applicable to large strain cyclic (reversal) loading. The material parameters might require minor adjustment, but no change in the model is necessary.

Hu, Rauch, and Teodosiu (1992) performed large strain torsional reversal test on AK-mild steel, Fig. 4-11. They found that a plateau on the stress-strain curve commences right after yielding on strain reversal. In this regime, the material exhibits very small hardening.

The softening is more pronounced if the reversal happened at a larger strain level. To check if we can predict the same phenomena from our model, we simply simulate the same test with parameters for copper, and the result is shown in Fig. 4-12. We are pleased to report that the qualitative features of their experimental curves are well-captured by our model.

4.4.2 Strain path change test

Rauch and Schmitt (1989) also performed strain-path-change test on mild steel. They pre-deformed samples of thin plates in tension, then cut square pieces out of it with different orientations α to conduct a second step simple shear test, Fig. 1-7. By changing the relative orientation α of the shear sample to the tension sample, they were able to perform two-step, strain-path-change tests.

The special test which shows different results from the others experiments concerning the Bauschinger effect is the one for which $\alpha = 90^o$. When α equals 90^o, instead of getting reduction in yielding, the second stage shows an increase in the yield strength.

We also perform a simulation of load path change test to see if our model can capture such feature. The results are shown in Fig. 4-13. We are very pleased to see that although the response for $\alpha = 45^o$ overshoot a little at the beginning of the reloading[3], both the additional hardening ($\alpha = 90^o$) accompanied by softening ($\alpha = 135^o$) are well captured by the current model. This results support our positive comment on a physically based, two-parameter crystal plasticity model in Chap. 1, and demonstrate the applicability of our model for general path-change simulations.

[3]The time-integration procedure could be possibly improved to eliminate this spike.

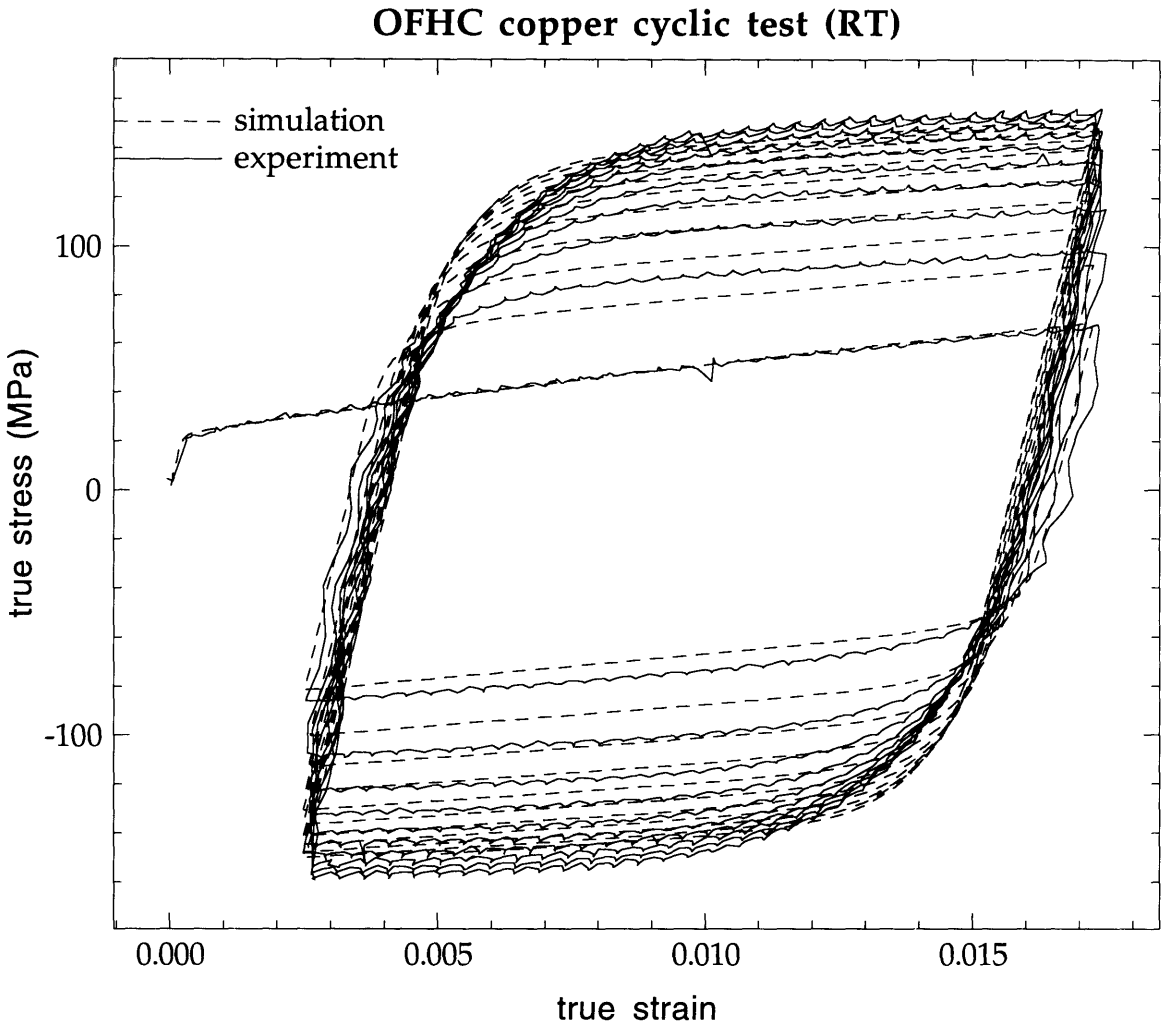

Figure 4-1: Unsymmetric strain cycling test, $\epsilon = 1\% \pm 0.75\%$.

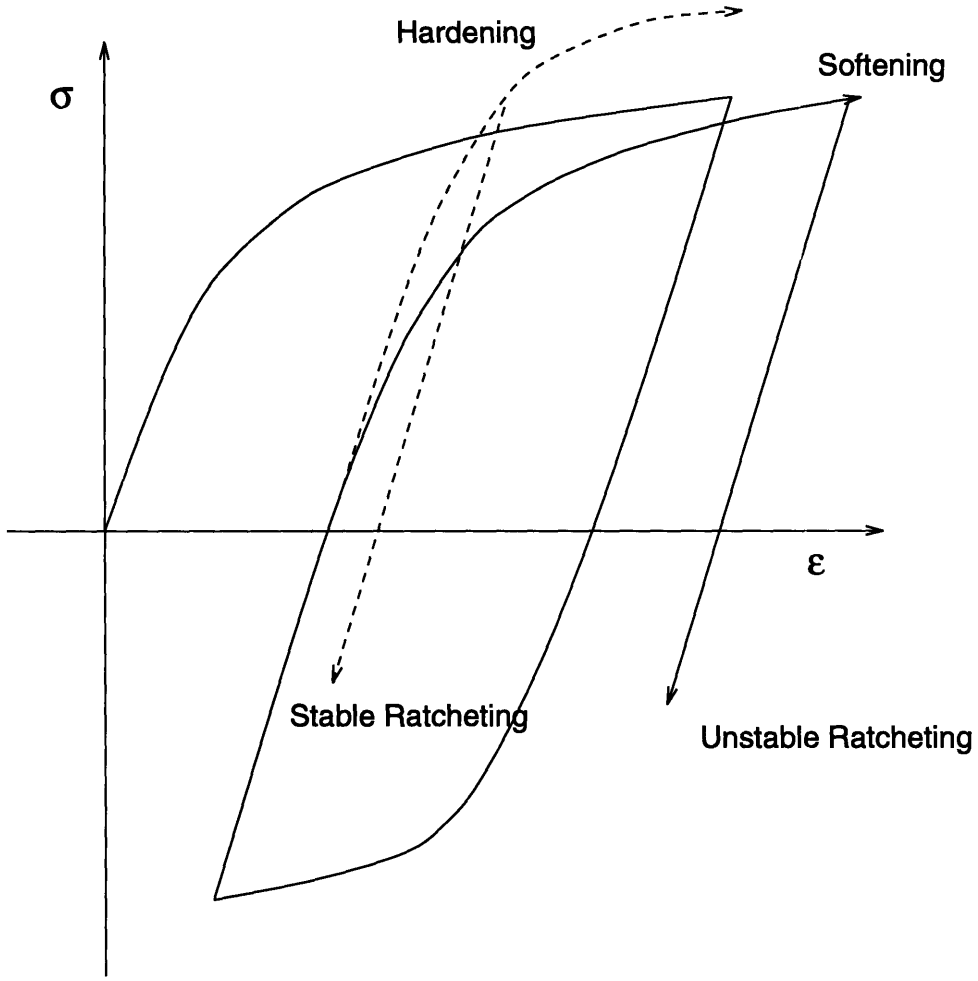

Figure 4-2: Schematic drawing shows the role of hardening in determining the ratcheting and relaxation behavior during cyclic deformation.

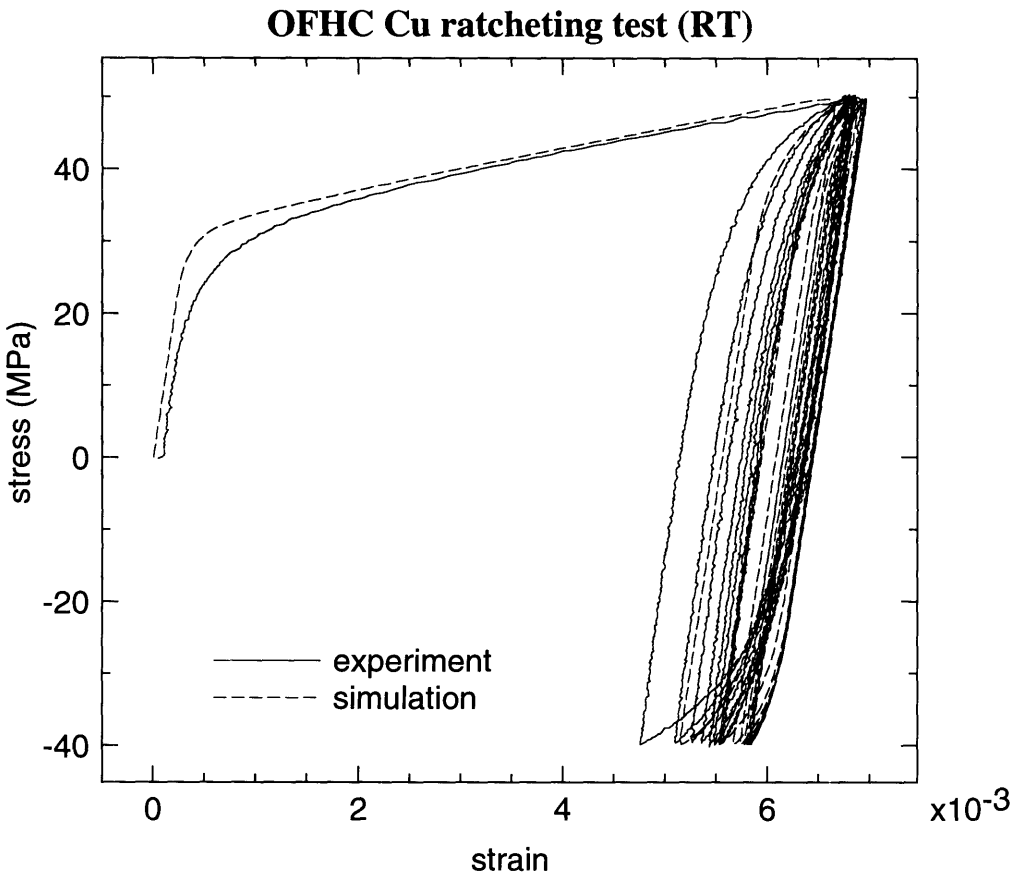

Figure 4-3: Ratcheting test.

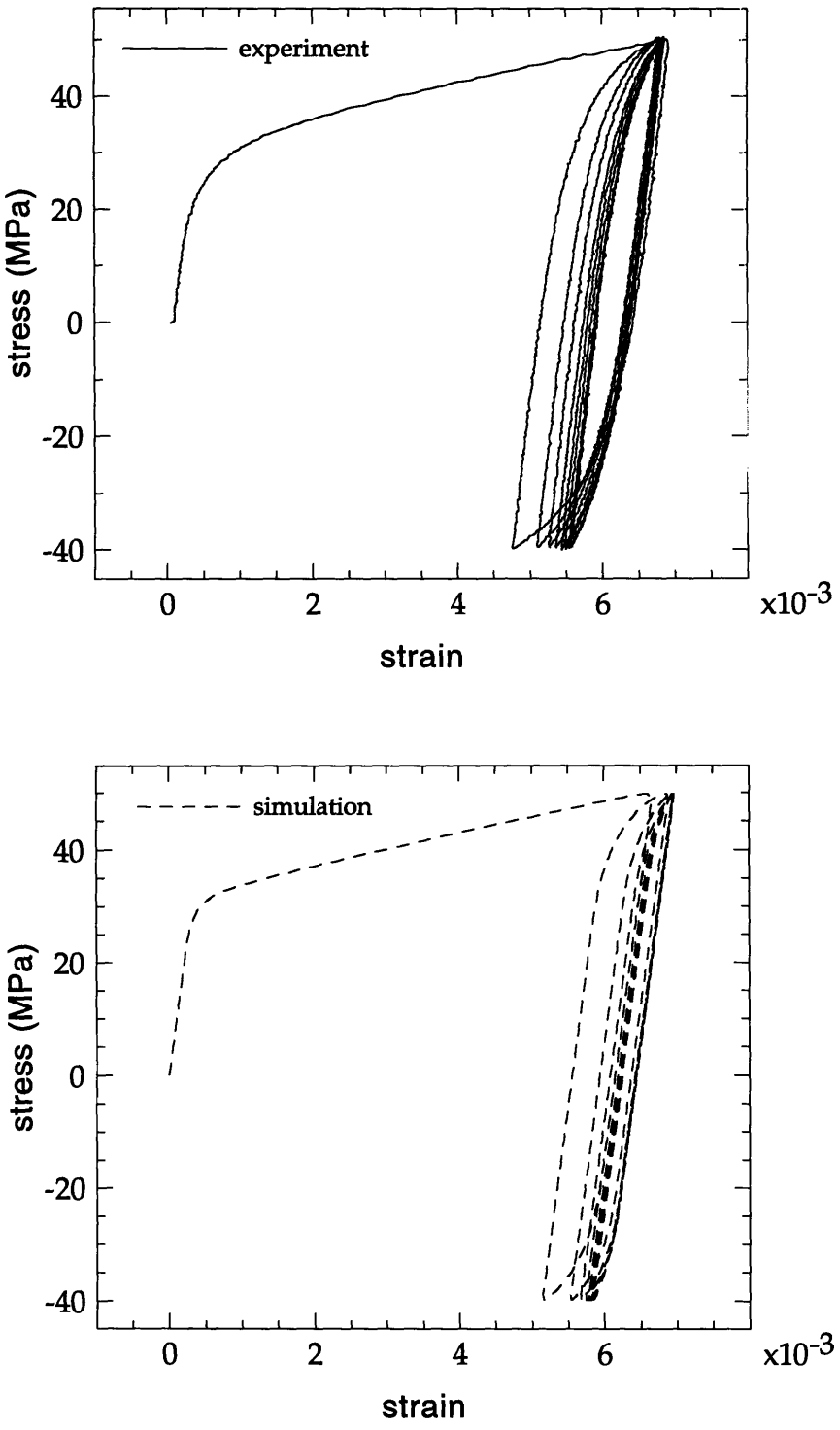

Figure 4-4: Ratcheting test. Same data as in the last figure but the expermental result and the simulation are plotted separately.

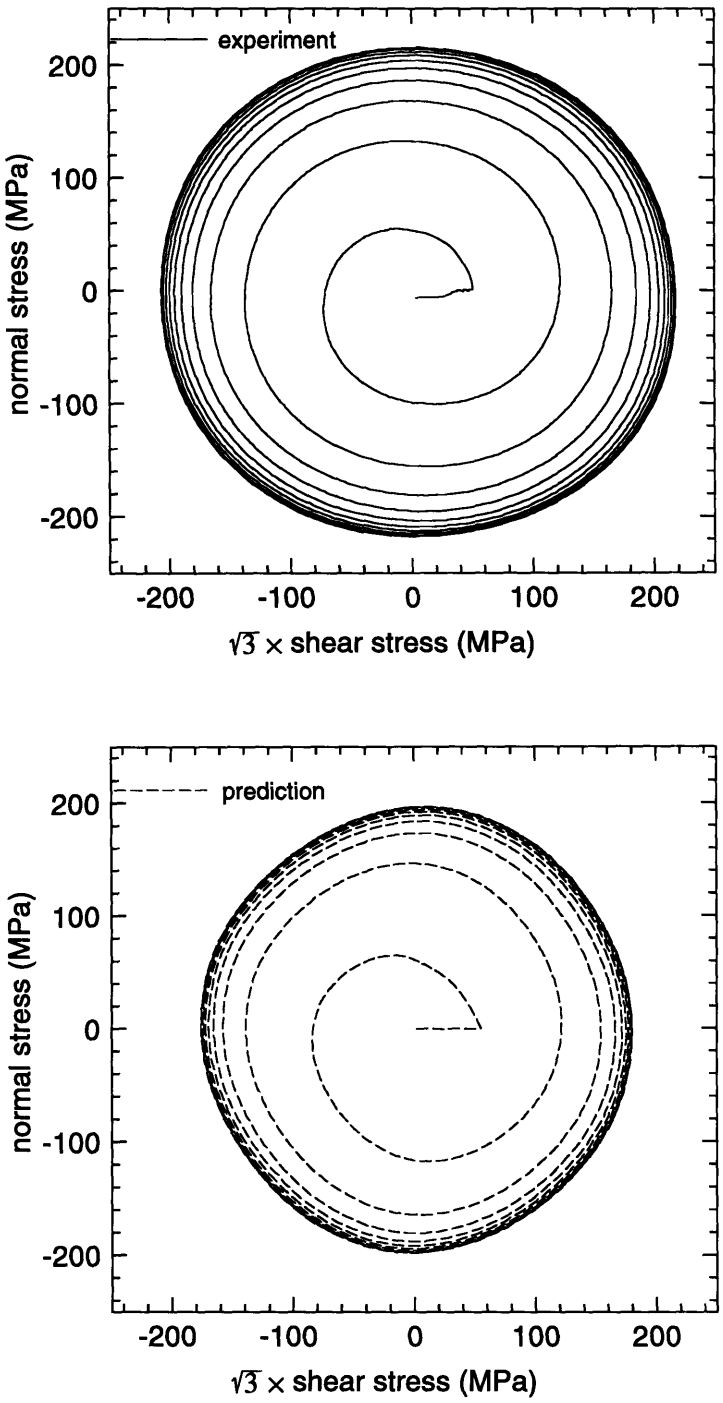

Figure 4-5: 90^o out of phase biaxial cyclic test ($\bar{\epsilon}_a = 1\%$, shearing first).

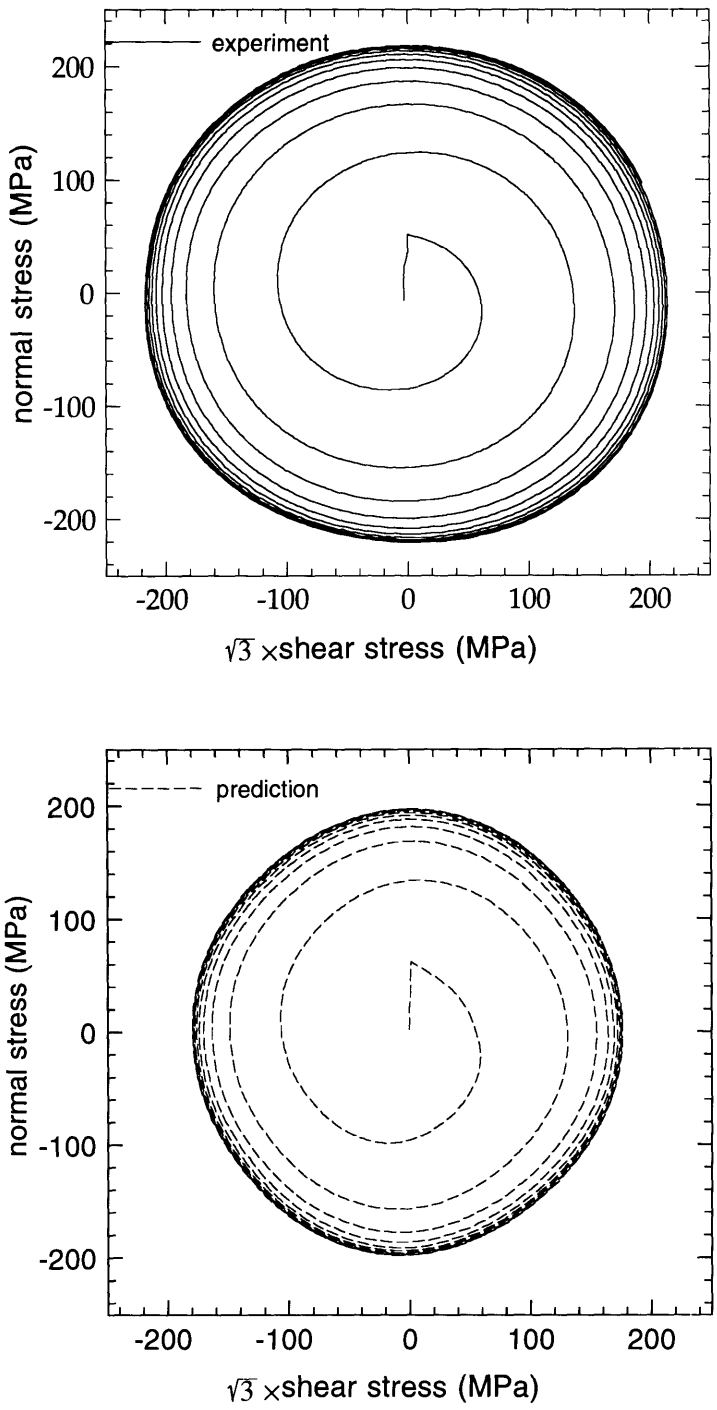

Figure 4-6: 90^o out of phase biaxial cyclic test ($\bar{\epsilon}_a = 1\%$, tension first).

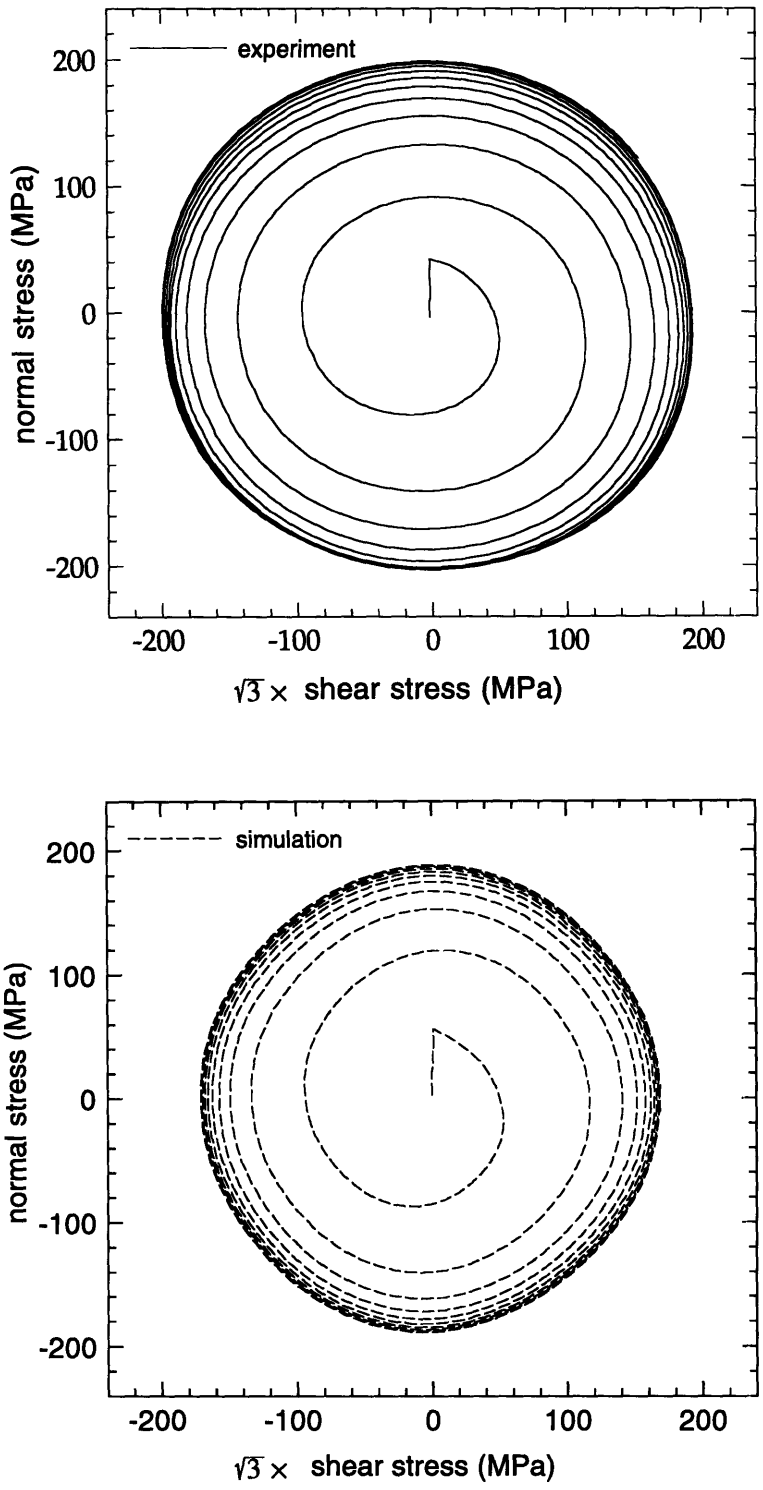

Figure 4-7: 90^o out of phase biaxial cyclic test, $\bar{\epsilon}_a = 0.82\%$.

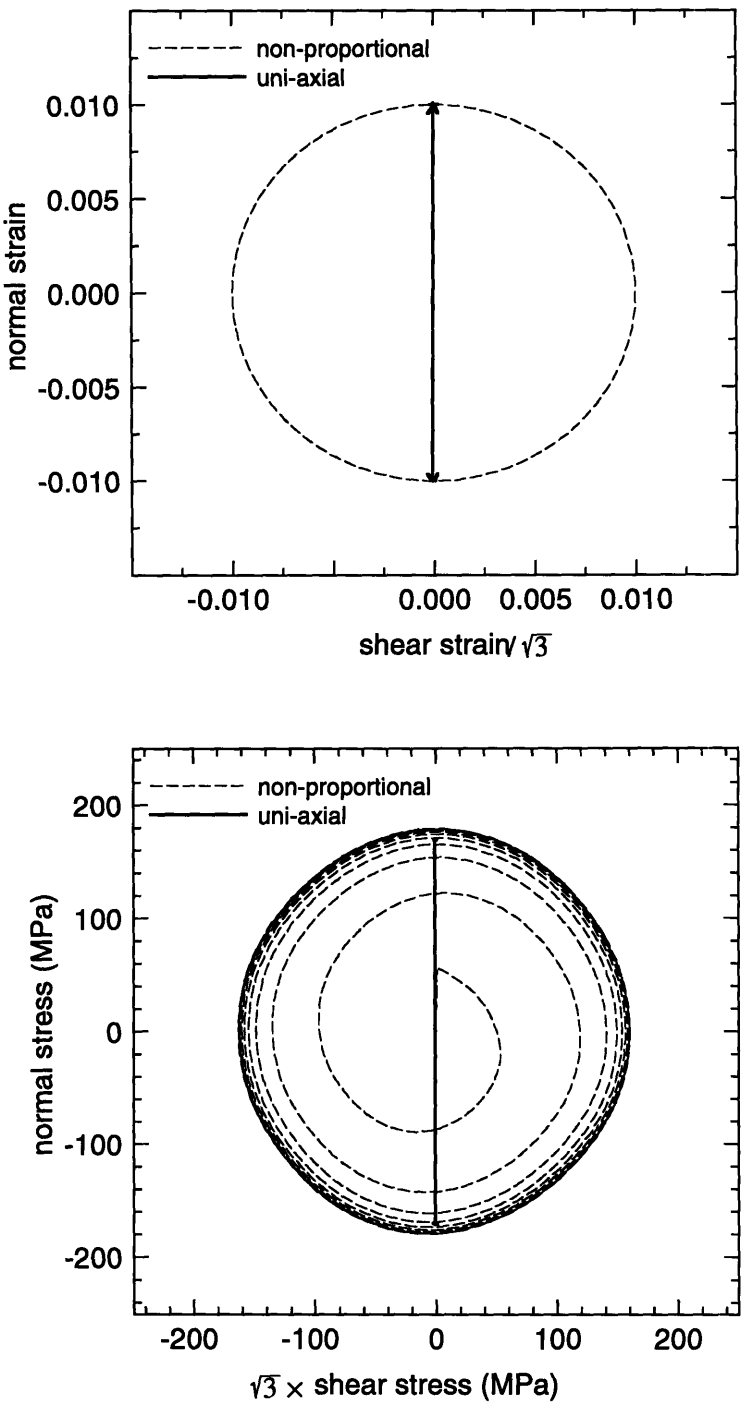

Figure 4-8: Comparison of the saturation stress level between uniaxial and non-proportional 90^o out-of-phase cyclic test with the same equivalent strain amplitude. (results from simulation)

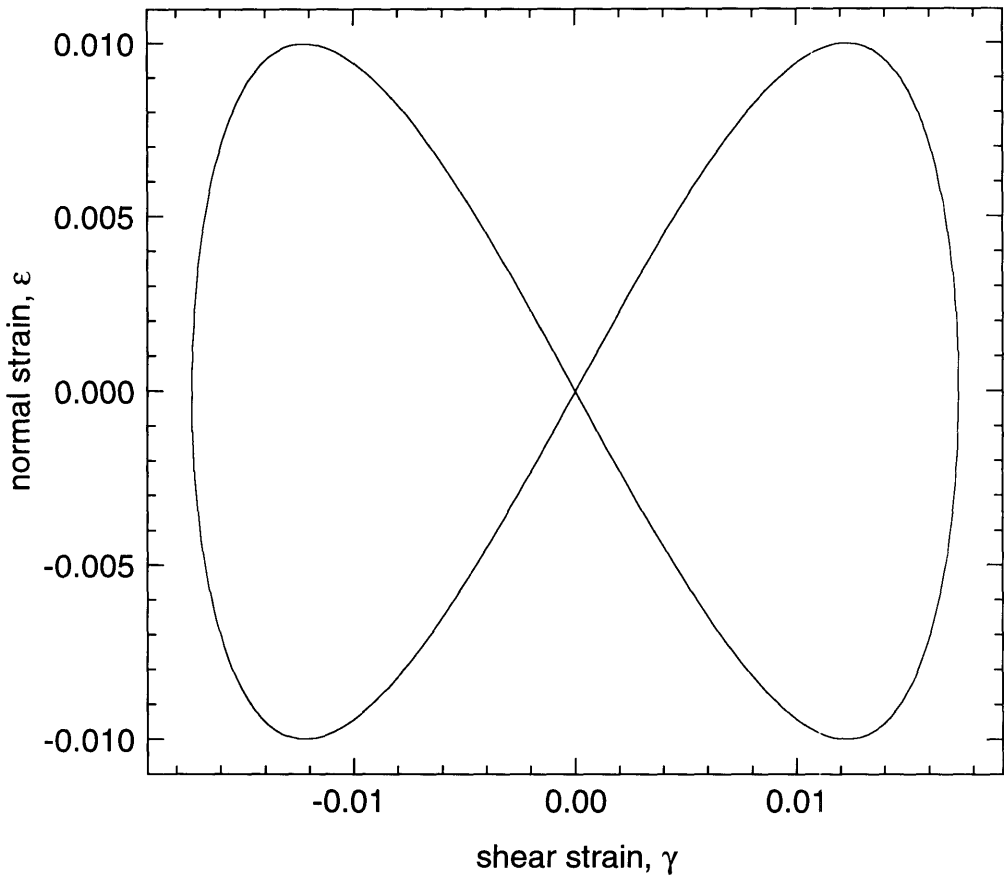

Figure 4-9: Strain path in a "butterfly" cyclic experiment.

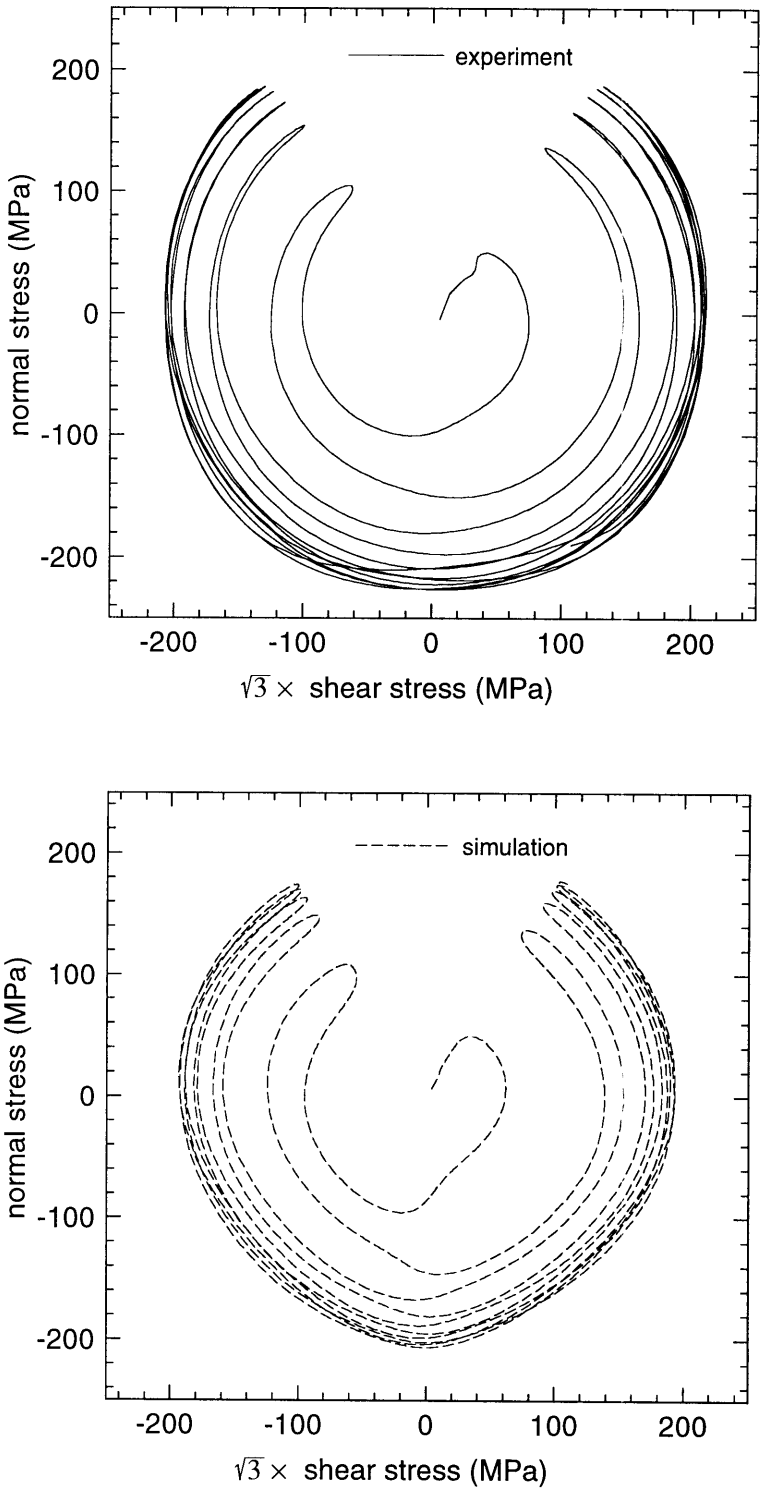

Figure 4-10: Butterfly test

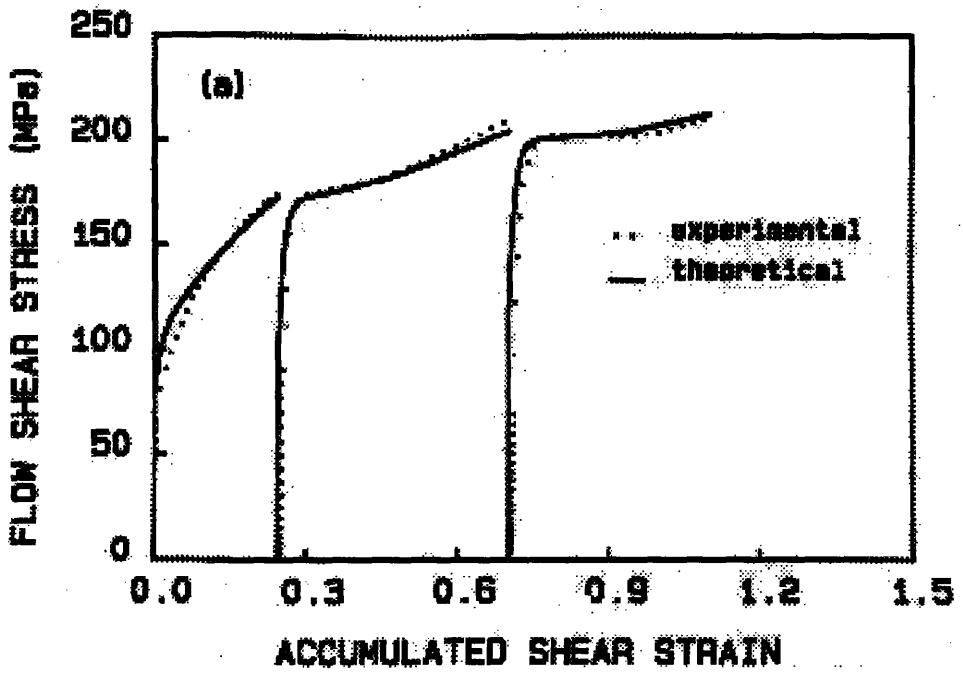

Figure 4-11: Large strain reversal torsion test, (Hu, Rauch, and Teodosiu, 1992).

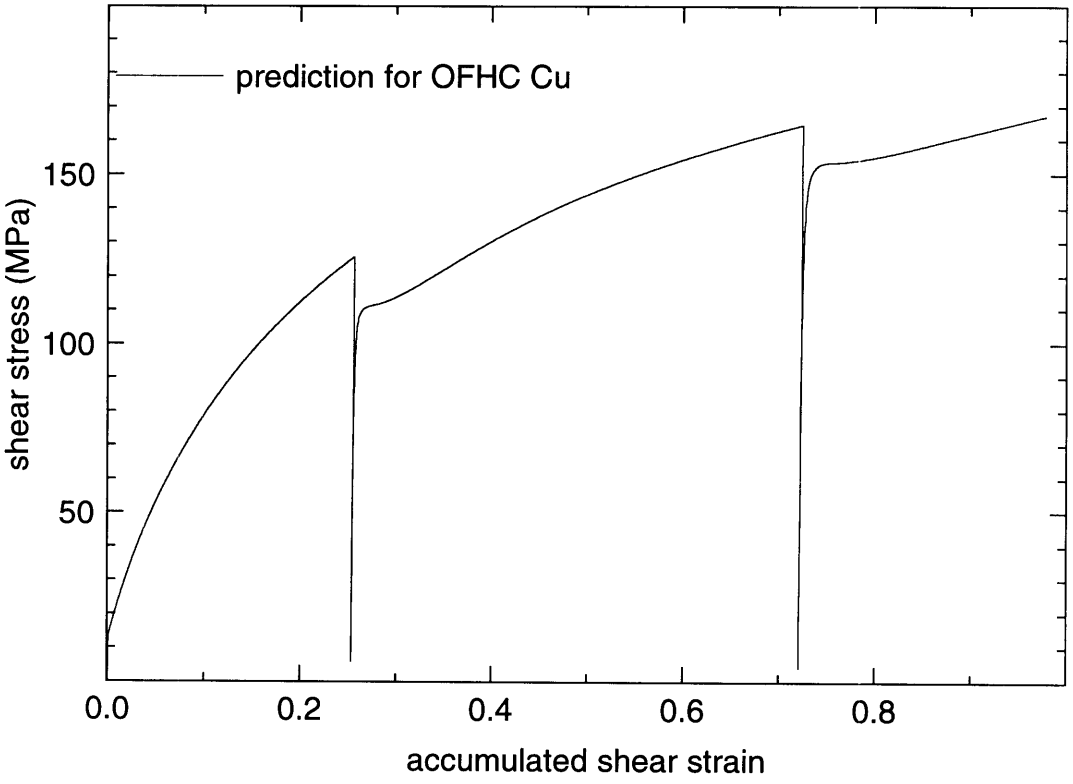

Figure 4-12: Simulation of large strain reversal torsion test.

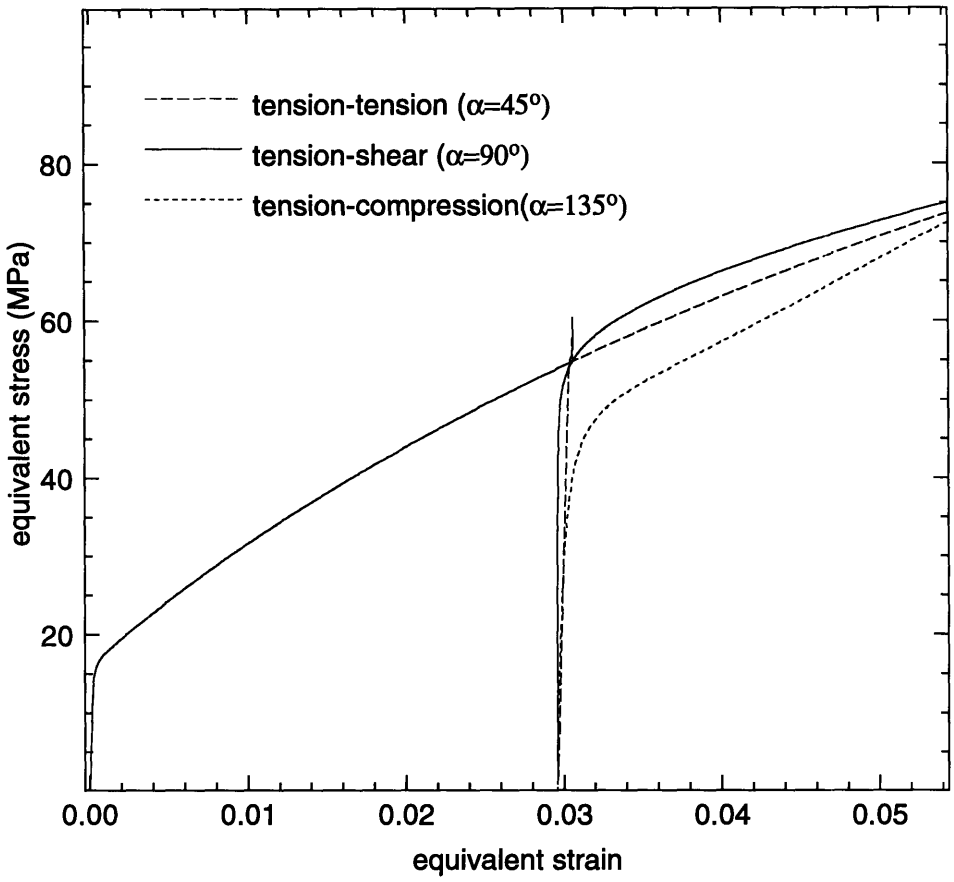

Figure 4-13: Simulation of strain-path-change test

Chapter 5

Closure

With the background of the crystal plasticity model of Kalidindi, Bronkhorst, and Anand (1991) and kinematic-isotropic hardening model White and Anand (1989), the following have been accomplished in the present study:

1. A combined kinematic-isotropic hardening crystal plasticity model applicable to cyclic loading has been developed. Such a model, with physically based internal variables, s^{α} and x^{α}, can capture both the crystallographic slip and the substructure evolution in a continuum level formulation.

2. A fully implicit time-integration procedure has been developed for the above model and implemented in the finite element code ABAQUS to facilitate simulations of cyclic deformations for FCC materials.

3. A set of cyclic experiments including uniaxial symmetric and unsymetric strain cycling, uniaxial unsymmetric stress cycling, biaxial strain cycling has been performed on OFHC Copper from the fully annealed state. For the tremendous hardening effect of the annealed copper (saturation stress is about ten times higher than the yield stress), the experiment results provide a set of challenging data resource to test the robustness of any plasticity model.

4. A new set of evolution equations for the back stress variable is defined. Simulations based on these equations capture the monotonic macroscopic cyclic stress/strain response very well, with cyclic strain range varies from 0.3% to 3%. The biaxial response is also reasonably captured considering the difficulties of determining true strain for a position controlled test.

Although the motivation of the current study comes from our long-term objective of contructing a cyclic plasticity model for Ni-base superalloys, the presented combined hardening crystal plasticity model also stand by itself as a good cyclic plasticity model for pure FCC metals. The main difficulty of the current model lies in the underprediction for the biaxial cases, possibly caused by an oversimplified latent hardening relationship. The assumption of no interaction of softening between different slip systems might be expedient so as to reduce calculation time, but it is questionable in reality. Considering the good predictability of the current model, we are reasonably satisfied with the current latent-hardening relations; however, further insight into the mechanisms would be beneficial.

Further, the current continuum model incorporates an important softening phenomena of s^α during reverse deformation. It would be interesting to investigate the proper forms for the hardening parameters h_1, h_2, and h_3 (Eqn. 2.5, 2.32) based on dislocation interactions, and also the coupling relationship between them, but we leave this complex task for the future.

Biliography

[1886] BAUSCHINGER, J., *On the Change of the Elastic Limit and Hardness of Iron and Steels through Extension and Compression, through Heating and Cooling, and through Cycling*, Mitteilung aus dem Mechanisch, Technischen Laboratorium der K. Technische Hochschule in Munchen, 13, Part 5, p. 31.

[1953] WOOLEY, R.L., *The Bauschinger Effect in Some Face-Centered and Body-Centered Cubic Metals*, Phil. Mag., 44, pp. 597-618.

[1954] EDWARDS, E.H. and WASHBURN, J., *Strain Hardening of Latent Slip Systems in Zinc Crystals*, Trans. AIME, 200, p. 1239.

[1962] DEAK, G., *A Study of the Causes of the Bauschinger Effect*, Sc.D. Thesis, Dept. of Mechanical Engineering, MIT, Cambridge, MA.

[1965] PHILLIPS, A. and SIERAKOWSKI, R.L., *On the Concept of Yield Surface*, Acta Mechanica, 1, p. 29.

[1967] JACKSON, P.J., and BASINSKI, Z.S., *Latent Hardening and Flow Stress in Copper Single Crystals*, Canadian J. Physics, 45, p. 707.

[1967] MORZ, Z., *On the Description of Anisotropic Work Hardening*, Acta Mechanica, 21, p. 173.

[1970] HUTCHINSON, J.W., *Elastic-Plastic Behavior of Polycrystalline Metals and Composites*, Proc. R. Soc. Lond., A319, p. 247.

[1971] MARUKAWA, K. and SANPEI, T., *Stability of the Work Hardened State Against Stress Reversal in Copper Single Crystals*, ACTA Metallurgica, 19, pp. 1169-1176.

[1971] SIMMONS, G. and WANG, H., *Single Crystal Elastic Constants and Calculated Aggregate Properties*, The M.I.T. Press, Cambridge, MA

[1972] PHILLIPS, A. and KASPER, R., *The Effect of Loading Path on the Yield Surface at Elevated Temperatures*, International Journal of Solids Struct., 9, p. 379.

[1975] DAFALIAS, Y.F. and POPOV, E.P., *A Model of Nonlinearly Hardening Materials*

for Complex Loading, Acta Mechanica, 21, pp. 173-192.

[1975] HASEGAWA, T., YAKOU, T. and KARASHIMA, S., *Deformation behaviour and Dislocation Structures upon Stress Reversal in Polycrystalline Aluminium*, Material Science and Engineering, 20, pp. 267-276.

[1976] DAFALIAS, Y.F. and POPOV, E.P., *Plastic Internal Variables Formalism of Cyclic Plasticity*, ASME Journal of Applied Mechanics, 43, pp. 645-651.

[1979] HASEGAWA, T. and KOCKS, U. F., *Thermal Recovery Processes in Deformed Aluminum*, Acta Metallurgica, 27, pp. 1705-1716.

[1979] WENG, G.J., *Kinematic Hardening Rule in Single Crystals*, International Journal of Solid Struct., 15, p.861.

[1980] HASEGAWA, T. and YAKOU, T., *Effects of stress Reversal and Thermal Recovery on Stress vs Strain Behavior in Aluminum*, Scripta Metallurgica, 14, pp. 1083-1087.

[1980] WENG, G.J., *Dislocation Theories of Work Hardening and Yield Surfaces of Single Crystals*, Acta Mechanica., 37, p.217.

[1982] PEIRCE, D., ASARO, R.J. and NEEDLEMAN, A., *An Analysis of Nonuniform and Localized Deformation in Ductile Single Crystals*, Acta Metallurgica, 30, p.1087.

[1983] PEIRCE, D., ASARO, R.J. and NEEDLEMAN, A., *Material Rate Dependence and Localized Deformation in Crystalline Solids*, Acta Metallurgica, 31, pp. 1951-1976

[1984] CAILLETAUD, G., KACZMAREK, H. and POLICELLA, H., *Some Elements on Multiaxial Behaviour of 316L Stainless Steel at Room Temperature*, Mechanics of Materials, 3, pp. 333-347.

[1985] ANAND, L., *Constitutive Equations for Hot-Working of Metals*, International Journal of Plasticity, 1, pp. 203-231.

[1985] ASARO, R.J. and NEEDLEMAN, A., *Texture Development and Strain Hardening in Rate Dependent Polycrystals*, Acta Metallurgica, 33, pp. 923-953

[1985] BASINSKI, Z.S., BASINSKI, S.J. and HOWIE, A., *Early Stages of Fatigue in Copper Single Crystal*, Philosophical Magazine, 19, 899-924.

[1986] CHRISTODOULOU, N., WOO, O.T. and MacEWEN, S.R., *Effect of Stress Reversals on the work Hardening behaviour of Polycrystalline Copper*, Acta Metallurgical, 34, pp. 1553-1562.

[1987] WENG, G.J., *Anisotropic Hardening in Single Crystals and the Plasticity of Polycrystals*, International Journal of Plasticity, 3, pp. 315-339.

[1988] DAME, L.T. and STOUFFER, D.C., *A Crystallographic Model for Nickel Base Single Crystal Alloys*, Journal of Applied Mechanics, 55, pp. 325-331.

[1988] WHITE, C.S., *A Combined Isotropic-Kinematic Hardening Model for Large Deformation Metal Plasticity*, Ph.D. Thesis, Massachusetts Institute of Technology, Cambridge, MA

[1989] BROWN, S., KIM, K, and ANAND, L., *An Internal Variable Constitutive Model for Hot Working of Metals*, International Journal of Plasticity, 5, pp. 95-130.

[1989] WALKER, K.P. and JORDAN, E.M., *Biaxial Constitutive Modelling and Testing of a Single Crystal Superalloy at Elevated Temperatures*, Biaxial and Multiaxial Fatigue, EGF 3, Mechanical Engineering Publications, London, pp. 145-170.

[1989] RAUCH, E.F. and SCHMITT, J.H., *Dislocation Substructures in Mild Steel Deformed in Simple Shear*, Materials Science and Engineering, A113, pp. 441-448.

[1990] STOUFFER, D.C., RAMASWAMY, V.G., LAFLEN, J.H., VAN STONE, R.H., and WILLIAMS, R., *A Constitutive Model for the Inelastic Multiaxial Response of Rene'80 at 871C and 982C*, Journal of Engineering Materials and Technology, 112, pp. 241-246.

[1990] WHITE, C.S., BRONKHORST C.A., and ANAND L., *An Improved Isotropic-Kinematic Hardening Model for Moderate Deformation Metal Plasticity*, Mechanics of Materials, 10, pp 127-147.

[1991] BRONKHORST, C.A., *Plastic Deformation and Crystallographic Texture Evolution in Face-Centered Cubic Metals*, Ph.D. Thesis, Massachusetts Institute of Technology, Cambridge, MA.

[1991] MERIC, L. and CAILLETAUD, G., *Single Crystal Modeling for Structural Calculations: Part2–Finite Element Implementation*, Journal of Engineering Materials and Technology, 113, pp. 171-182.

[1991] MERIC, L. POUBANNE, P. and CAILLETAUD, G., *Single Crystal Modeling for structural Calculations: Part 1–Model Presentation*, Journal of Engineering Materials and Technology, 113, pp. 162-170.

[1992] BRONKHORST, C.A., KALINDINDI, S.R. and ANAND, L., *Polycrystal Plasticity and the Evolution of Crystallographic Texture in the FCC Metals*, Phil. Trans. R. Soc. Lond. A, 341, pp. 443-477.

[1992] Hu, Z., RAUCH, E. F. and TEODOSIU, C., *Work-Hardening Behavior of Mild Steel*

under Dtress Reversal at Large Strains, International Journal of Plasticity, 8, pp. 839-856.

[1992] JORDAN, E.H. and WALKER, K.P., *A Viscoplastic Model for Single Crystals*, Journal of Engineering Materials and Technology, 114, pp. 19-26.

[1992] KALIDINDI, S.R., *Polycrystal Plasticity: Constitutive Modeling and Deformation Processing*, Ph.D. Thesis, Massachusetts Institute of Technology, Cambridge, MA.

[1992] KALIDINDI, S.R., BRONKHORST, C.A., and ANAND, L., *Crystallographic Texture Evolution in Bulk Deformation Processing of FCC Metals*, Journal of the Mechanics and Physics of Solids, 40, 3, pp. 537-569.

[1992] SHERWOOD, J.A. and STOUFFER, D.C., *A Phenomenologically Based Constitutive Model for Rene 95*, Transactions of the ASME, 114, pp. 340-347.

[1992] TVERGAARD, V., *Application of Plastic Material Models*, Proceedings of the 13th Riso International Symposium on Materials Science: Modelling of Plastic Deformation and Its Engineering Applications, Riso National Laboratory, Roskilde, Denmark.

[1994] ALLAN, C.D., *Plasticity of Nickel Base Single Crystal Superalloys*, Ph.D. Thesis, Massachusetts Institute of Technology, Cambridge, MA.

[1994] HASSAN, T. and KYRIAKIDES, S., *Ratcheting of Cyclically Hardening and Softening Materials: II, Multiaxial Behavior*, International Journal of Plasticity, 10, 2, pp. 185-212.

[1994] LIU, C.D., YOU, D.X. and BASSIM, M.N., *Cyclic Strain Hardening in Polycrystalline Copper*, ACTA Metall. Mater., 42, pp.1631-1638.

[1994] KHAN, A.S. and SU, X.M., *Constitutive Relations for Single Crystal Based on Two Surface Description*, International Journal of Plasticity, 10, pp. 807-823.